Humboldt-Universität zu Berlin
Institut für Physik
Newtonstrasse 15, 12489 Berlin

Space Charge Effects in Cascaded HGHG-FELs

Diplomarbeit

Lutz Hein

geb. am 09.09.1982 in Stralsund

Zusammenfassung

Der Freie Elektron LASER (FEL) hat sich bereits als die vierte Generation der Synchrotron-Lichtquellen etabliert. Durch seine speziellen Eigenschaften bietet er bislang einzigartige Anwendungsmöglichkeiten in Forschung und Entwicklung. In diesem Zusammenhang gewinnen besonders kurze Pulse mit hohen Photonenenergien, also kurze Wellenlängen, immer mehr an Bedeutung. Deshalb sind gegenwärtig FEL-Quellen im Gespräch, die diese kurzen, hochenergetischen Strahlen bieten. Der kaskadierte HGHG-FEL, der unter anderem für BESSY-FEL, STARS [1],[2], und für FLASH II [3],[4], vorgesehen wurde, ist ein viel versprechendes Konzept. Im Allgemeinen werden die höheren Spitzenbrillanzen, die charakteristisch für FEL-Strahlung sind, durch höhere Spitzenströme pro Elektronenpaket (Bunch) erzeugt. Dabei sind hohe Bunchladungen wie z.B. 2.5nC bei einer Teilchenenergie von 2.3 GeV für den BESSY-FEL üblich. Bei derart hohen Ladungsansammlungen können die Wechselwirkungen der Elektronen untereinander und mit ihrer Umgebung nicht mehr vernachlässigt werden. Der Bunch in kaskadierten HGHG-Strukturen ist für mehrfache Seed- und Emissionsprozesse ausgelegt, wodurch im Allgemeinen die Bunchlänge viel größer als der Bunchquerschnitt ist. Auch werden immer höhere Teilchenenergien angestrebt. Jedoch haben die transversalen und longitudinalen Raumladungskräfte einen nicht zu vernachlässigenden Einfluss auf die Entwicklung der Buchdimensionen und somit auf die FEL-Strahlqualität. Die Untersuchung von Raumladungseffekten erfolgt mit Simulationsprogrammen. Da der Einsatz von "Teilchen Tracking"-Programmen, wie ASTRA und GPT, sehr CPU-zeitintensiv ist, wurde für schnelle Abschätzungen der Raumladungseffekte in kaskadierten HGHG-FEL Strukturen im Rahmen dieser Arbeit das Programm P12 entwickelt. P12 verarbeitet die Effekte der transversalen Raumladung in linearer Strahloptik, wodurch die Entwicklung der Bunchdimensionen entlang der Strahloptik (Lattice) beobachtet werden können. In kombinierter Anwendung von P12 mit anderen Simulationsprogrammen lassen sich die verschiedenen Ordnungen der Raumladungseffekte unterscheiden und geeignete Kompensationsmethoden entwickeln. Im Folgenden werden die theoretischen Grundlagen für das Programm P12 beschrieben und die Annahmen, die bei der Erstellung von P12 nötig waren, werden in Detail aufgezeigt und Gründe für diese Nährungen erläutert. Da der Undulator ebenfalls ein optisches Element mit Fokussierungseigenschaften darstellt, wurden die Fokussierungseigenschaften der Undulatoren in spezielle Unterprozeduren berücksichtigt. Vergleiche der P12-Resultate mit den Resultaten gängiger Simulationsprogramme, wie ASTRA und Trace3D, beweisen die Anwendbarkeit des Programms P12. Abschließend wird anhand von Beispielen der Effekt der Raumladung auf die Ausgangsleistung von FELs, FLASH II and STARS, mit Hilfe des Programms Genesis1.3 demonstriert.

Abstract

Free Electron Lasers (FEL) have been already established as the fourth generation light-sources. Their characteristics offer unique possibilities for many applications in material science. In particular, there are a large number of experiments demanding short FEL pulses with high photon energies. Seeded FEL-schemes provide this superior radiation. Such a promising FEL-scheme is the multi-stage HGHG-structure (*High Gain Harmonic Generation*), which is proposed for the BESSY-FEL, STARS, and FLASH II. In general, the high peak brilliance, which is a characteristic of a single pass FEL, is generated by a high peak current. So, a high bunch charge is needed, e.g. 2.5nC with an average particle energy of 2.3GeV for BESSY FEL. At this very high charge density the interactions of the electrons with each other and their environment cannot be neglected anymore. In the HGHG-FEL scheme the bunch is generated for several seed and emission processes. Thus, the longitudinal dimension of the electron bunch is much bigger than the dimensions of its cross section. Furthermore, there are also higher average particle energies aspired. Nevertheless, the transverse and longitudinal space charge effects produce a significant impact on the development of the bunch properties as well as on the resulting FEL performance. For the investigation of the space charge effects simulation programs are required. Since the use of particle tracking programs, like ASTRA and GPT, is very CPU time-consuming, a program for fast estimations of space charge effects in multi-stage HGHG-FELs was required. As a result of this work the program P12 for the fast estimations of space charge effects at multi-stage HGHG-FEL is developed. It copes with transversal space charge effects in a linear manner, whereby the development of the bunch dimensions can be observed. The combined employment of P12 and other space charge calculating programs allows to distinguish different orders of space charge effects and to develop techniques for their compensation. In the following the theory used for creating the program P12 is presented and the assumptions underlying P12 are discussed in detail as well as the motivation to use them.

Since the FEL-process takes place in undulators, the optical features of undulators have to be recognised as well. Special subroutines in P12 cope with the undulator focusing in different selectable regimes, which are also discussed. The comparison of the results of P12 with the results of established space-charge calculating programs, like ASTRA and Trace3D, proves the applicability of P12. The impact of the transversal space charge effects on the performance of the FELs FLASH II and STARS is demonstrated with Genesis1.3 in the concluding section.

Contents

1

Introduction

Nowadays, Free Electron Lasers (FEL) are established in the ensemble of light-producing devices. Especially the single-pass high-gain FELs are of particular interest for modern experiments. The single-pass FEL radiation-output is generally characterised by an extreme high peak brilliance and short pulse length. Furthermore, in dependency of the layout of the facility, it is tunable in wavelength and in polarisation. Due to these features new experiments are possible.

The observation of molecular oscillations in IR-range needs extreme high intensity [5], whereby the use of FELs is enforced. Another application is the research of fast running biological process in X-ray regime [6],[7]. X-ray radiation damages biological materials and therefore it influences the biological processes. Sufficient high intensity shortens the exposure time and offers the possibility for an instantaneous photography of the current process. In addition there are also proposals for X-ray-holography [7], whereby a high coherence is required, which is given by using seeded FEL radiation. Not only the number of FEL applications increases rapidly, but the demands on the performance of FELs increases as well. The properties of the FEL output depend sensitively on the characteristics of the electron beam. The working principle of the FEL bases on the fact, that electrons and radiation interact. In general, this takes place in an undulator, which is an alternating sequence of dipole magnets. The main task of this magnetic arrangement is to change the transversal velocity of electrons. So the electrons can couple to the transversal component of the radiation electric field. This interaction causes an energy transfer between electrons and radiation field. Electrons can win or loss energy depending of their phase. In general, both effects occur at the same time, but with different efficiency depending on the radiation.

A criterion of the FEL performance is the 'Pierce'-parameter, which provides informations about the efficiency of the FEL-interaction. The Pierce parameter is a function of the electron density, undulator parameter and the average electron energy [8]. The electron density is influenced on its way from the rf-gun to the FEL-undulators. Its generation and acceleration are particularly crucial. Inside the 'gun', electrons are emitted from a cathode and accelerated by rf-fields. This initial charge distribution has already an effect on the later FEL-process, as it limits the minimum possible beam emittance. The bunch is accelerated by rf-fields, which can be used to establish an energy chirp along the bunch. This energy chirp is utilised for 'bunch compression', which increases the charge density. The high charge density gives rise to another unwanted effect: the space charge

effect. It is the interaction of charged particles inside the bunch with each other and with their environment. In general, the particle position inside the bunch determines the space charge force experienced by a single particle. The relationship between particle position and space charge force is only in special rare cases linear. Space charge effects, like repulsing forces of electro-magnetic fields and image charges, cause an expansion of the bunch. In order to compensate these expansions, focusing elements have to be adapted in the layout of the facility. With the help of fast calculating, analytical programs the impacts of space charges can be estimated and compatible modifications of the layout can be created. Afterwards the modifications have to be tested in detail with computationally-expensive particle-tracking programs. The results of these programs are marked by the underlying approximations and assumptions. The scope of this work is the investigation of the transversal space charge effects in the FEL-undulator-sections. Although tracking programs can be used for this investigation and for lattice design, they are less suitable, due to their CPUs-time-cost. Therefore, as a part of this work the simulation program 'P12' is created, which serves as a fast calculating program to investigate and to design the lattice layout of the undulator sections of FEL-facilities. In addition to the estimation of transversal space charge effects another application area of P12 is the simulation of the effect of undulator focusing on the optic. The beam optics including space charge effects as well as a detailed view of undulator optics is given in the second chapter. Chapter three describes details of the program P12. In the fourth chapter the results of the space-charge calculations of P12 are compared to the results of established programs. The impact of transversal space charge effects at HGHG-FEL is investigated in the fifth chapter. In the final sixth chapter a conclusion is given. In the appendix detailed discussions and developments of particle optics, a review of features of different distributions and a short description of the field distribution of the triaxial uniform charged ellipsoid are presented.

2

Theory

The scope of this work is the investigation of the impact of transversal space charge effects on beam optics in FELs. These effects have to be considered for lattice design and performance calculations. Obviously, a prerequisite for space charge calculations in accelerators is the computation of particle beam optics without space charge effects. Thus, the first part presents briefly basics of particle optics. It summarises a detailed discussion of particle optics, which is given in app. A, and describes the impact of different beam optic elements on particle beams. The second part of this chapter deals with the treatment of undulators in beam optics. Undulators are main components of every Free Electron LASER (FEL). In those elements the interaction of particle beam and light takes place. Undulators are magnetic devices, whose field configuration induce a continuous change of the propagation direction. The performance of FELs depends on the path of electrons through the undulator as well as the properties of the bunch. Moreover, undulators are also optical elements, whose characteristics influence the development of bunch dimensions. These optical features are discussed in the second part of this chapter. At the beginning of the third part an introduction presents different kinds of space charge effects. A review of different regimes of collective space charge effects and their approximations in simulations are given. In analytical simulations the model of the 'equivalent beam' is often used. It is based on a beam model with an uniform charge distribution. This model as well as its connection to real beams is presented in the following. Afterwards, different techniques of implementation of space charge effects in simulation programs are discussed. These techniques leads to special treatments of coupling elements. The bending magnet, as an example of coupling elements, is discussed in more detail.

2.1 Particle Optics

Influencing the motion of charged particles by the means of electro-magnetic fields is the subject of the accelerator physics. Using these fields, a bunch of charged particles can be accelerated, decelerated, bended, focused and defocused. The solution to the equation of motion of charged particles in electro-magnetic fields is used to define particle optics. The linearised equations of motion in transversal planes are given by:

$$x''(s) + \left(\frac{1}{R^2(s)} - k_x(s)\right)x(s) = \frac{1}{R(s)}\frac{\Delta p}{p}, \tag{2.1}$$

$$y''(s) + k_y(s)y(s) = 0. \tag{2.2}$$

Note that, a comoving coordinate system is used. R and k are parameters of optic elements and stand for curvature radius R and focusing strength k. The equations above are valid for each element (drift, bend,...) in a linear manner. They can be solved once the specific characteristic of the considered magnetic element, e.g. focusing strength, is given. It is convenient to use the matrix formalism to calculate the effect of these elements on a particle in the 6-dimensional phase space (two canonical coordinates in each of the three dimensions). A detailed derivation is presented in [9]. In the following the impacts of the most relevant elements, drift, bend and quadrupole, are described.

Drift

The element 'drift' describes a space without external fields. Thus, single particles will not experience any kind of redirection. The particle momentum remains constant. In a drift the deviation of the particle coordinates to the coordinates of the reference particle induces only displacements. The development of the particle coordinates due to a drift can be described by the following matrix.

$$R_{Drift} = \begin{pmatrix} 1 & L & 0 & 0 & 0 & 0 \\ 0 & 1 & 0 & 0 & 0 & 0 \\ 0 & 0 & 1 & L & 0 & 0 \\ 0 & 0 & 0 & 1 & 0 & 0 \\ 0 & 0 & 0 & 0 & 1 & \frac{L}{\gamma^2} \\ 0 & 0 & 0 & 0 & 0 & 1 \end{pmatrix} \tag{2.3}$$

Bend

Often in accelerators the design trajectory has to be a closed loop. The necessary bending is achieved by dipole magnets, short bends. In first approximation a bend is realized by a homogeneous magnetic field. The change of particle coordinates induces a focusing effect, called 'weak focusing'. There is also a dispersion effect, i.e. particles with different energies move on different paths through the bend. The following matrix describes the impact of a sector magnet, short Sbend. This kind of bend realized, if the beam enters and leaves the magnetic field perpendicular. If a beam did not enter perpendicular, particles with displacements take a different path through the bend. Due to the additional pathlength another focusing effect occurs, called 'edge' focusing, see app. A:

$$\tag{2.4}$$

$$R_{SBend} = \begin{pmatrix} cos(\frac{s}{R}) & Rsin(\frac{s}{R}) & 0 & 0 & 0 & R(1-cos(\frac{s}{R})) \\ \frac{-1}{R}sin(\frac{s}{R}) & cos(\frac{s}{R}) & 0 & 0 & 0 & sin(\frac{s}{R}) \\ 0 & 0 & 1 & s & 0 & 0 \\ 0 & 0 & 0 & 1 & 0 & 0 \\ -sin(\frac{s}{R}) & -R(1-cos(\frac{s}{R})) & 0 & 0 & 1 & -\frac{s}{\gamma^2} + (Rsin(\frac{s}{R})-s) \\ 0 & 0 & 0 & 0 & 0 & 1 \end{pmatrix}.$$

R is the curvature radius,
s is the pathlength along the trajectory,
$\frac{s}{R}$ corresponds to the bending angle as well as the bending phase,
γ is the relativistic gamma factor,

$$R_{edge} = \begin{pmatrix} 1 & 0 & 0 & 0 & 0 & 0 \\ \frac{tan(\varphi)}{R} & 1 & 0 & 0 & 0 & 0 \\ 0 & 0 & 1 & 0 & 0 & 0 \\ 0 & 0 & -\frac{tan(\varphi)}{R} & 1 & 0 & 0 \\ 0 & 0 & 0 & 0 & 1 & 0 \\ 0 & 0 & 0 & 0 & 0 & 1 \end{pmatrix} \tag{2.5}$$

The curvature radius R can be calculated from the field strength and particle energy. φ corresponds to the angle distinction of normal vector and beam propagation vector. The effect of edges can be focusing as well as defocusing. For the reference particle the longitudinal dimension of edges is infinitesimal [10]. Thus, the matrix elements R_{12}, R_{34} and R_{56} vanish. Rbends are composed of a combination of Sbends and edges.

Quadrupole

In contrast to a lens in light optics, quadrupoles focus in one of the transversal planes and defocus in the other one. A detailed description is also given in app. A. The following transfermatrix describes the impact of a quadrupole, which focuses in x-direction and defocuses in y-direction. In general, the focusing strength in one direction and the defocusing strength in the other are identical.

$$\tag{2.6}$$

$$R_{quadrupole} = \begin{pmatrix} cos(\varphi_x) & \frac{1}{\sqrt{|k_x|}}sin(\varphi_x) & 0 & 0 & 0 & 0 \\ -\sqrt{|k_x|}sin(\varphi_x) & cos(\varphi_x) & 0 & 0 & 0 & 0 \\ 0 & 0 & cosh(\varphi_y) & \frac{1}{\sqrt{|k_y|}}sinh(\varphi_y) & 0 & 0 \\ 0 & 0 & \sqrt{|k_y|}sinh(\varphi_y) & cosh(\varphi_y) & 0 & 0 \\ 0 & 0 & 0 & 0 & 1 & \frac{s}{\gamma^2} \\ 0 & 0 & 0 & 0 & 0 & 1 \end{pmatrix}$$

$\varphi_i = \sqrt{|k_i|}s$ stands for the focusing phase.

2.2 Undulators

Undulators are magnetic devices, used for generation of synchrotron-light. Due to their special field configuration, the charged particle are forced on a special trajectories through the undulator. They are 'wiggling' through the undulator. In an undulator the particles change continuously the direction of their propagation.
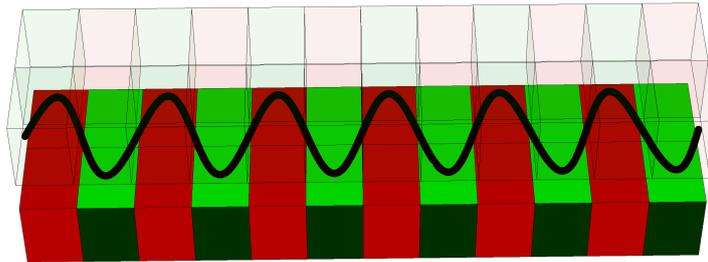
Figure 2.1:   Planar Undulator with a Possible Particle Path
The different magnetic poles are marked by different colours. A possible path of an electron beam is added (black curve).

For the production of synchrotron radiation electrons are used, because their mass is lower than the mass of other known charged single particles. The properties of the emitted light depend on the path of electrons through the undulator, i.e. it depends on the design of the undulator. The plane of polarisation of light is defined by the plane of the oscillating motion of the electrons. In a planar undulator the electrons 'wiggle' in one plane, figure 2.1, whereby the polarisation of light becomes linear. In the case of a helical motion inside the unduator the polarisation of light becomes elliptical or circular. Such a motion can be created for example by shifting of magnet rows as it is the case in APPLE-devices [11].
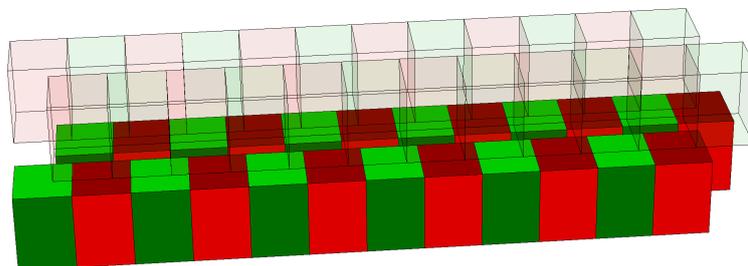
Figure 2.2:   Helical Undulator Design
The calibration of gapsize and shifting leads to complex field distributions, which can effect an elliptical motion of electrons.

The exact field configuration can become very complex. J.Bahrdt and G.Wüstefeld modelled exact field configurations in the transversal plane in 2×20 Fourier components [12]. Longitudinally, the magnetic field strength does not change in a pure sinusoid manner. The deviation from the pure sinus depends on the ratio of the undulator period length and gapsize. Self-evident, for an approximation in linear optics most of such higher order effects have to be neglected.

The schematic presentations of the undulators, figure 2.1 and figure 2.2, correspond to real devices. They consist of sequences of alternating Rbends. The fringing fields of the bends overlaps. In first order approximation those fringing fields are neglected. Thus, the undulator simplifiers to an alternating series of Rbends.

Rbend Approximation

In a first approach the complex field configuration of the undulator can be expressed as a series of Rbends. Each undulator period is modelled by four Rbend dipoles. The magnetic field strength of each bend is given by the undulator RMS K value [9].

$$K = \frac{eB_0\lambda_0}{mc^2 2\pi\sqrt{2}} \tag{2.7}$$

The RMS K value is also known as the 'Wiggle-/Undulatorparameter'. Electrons inside an undulator experience an alternating change of the bending forces. In a first approximation it comes to an oscillating change of the transversal particle position. The progress of change of the velocity is approximated by a wave with a maximum elongation, which depends on constant parameters, like period length λ_u, mass and average energy of electrons. Those parameters are combined to the undulator parameter. In contrast to Sbends the beam does not enter and/or leave the magnetic field perpendicular, so Rbends are marked by entrance and exit angles, see app. A. A beam enters the first Rbend perpendicular and leave with an angle of emergence, which is identical with the angle of bending. The next Rbend will be entered with the exit angle of the previous bend. Due to the alternating series of Rbends the electron beam 'wiggles' through the undulator. The weak focusing of the bends is (over)compensated by the effect of edge focusing. Thus, the plane of bending is featured by a weak defocusing. Furthermore, an additional advantage of the Rbend approach is, that the dispersion in an undulator is calculated implicitly correct in the linear manner. The corresponding matrices are already discussed in section 2.1. The approximation of elliptical undulators at the next subsection is similar to this Rbend approximation. For a comparison

of both approaches the following matrices are shown again.

$$R_{SBEND} = \begin{pmatrix} cos(\frac{s}{R}) & Rsin(\frac{s}{R}) & 0 & 0 & 0 & R(1-cos(\frac{s}{R})) \\ \frac{-1}{R}sin(\frac{s}{R}) & cos(\frac{s}{R}) & 0 & 0 & 0 & sin(\frac{s}{R}) \\ 0 & 0 & 1 & s & 0 & 0 \\ 0 & 0 & 0 & 1 & 0 & 0 \\ -sin(\frac{s}{R}) & -R(1-cos(\frac{s}{R})) & 0 & 0 & 1 & -\frac{s}{\gamma^2} + (Rsin(\frac{s}{R}) - s) \\ 0 & 0 & 0 & 0 & 0 & 1 \end{pmatrix}$$

$$R_{edge} = \begin{pmatrix} 1 & 0 & 0 & 0 & 0 & 0 \\ \frac{tan(\varphi)}{R} & 1 & 0 & 0 & 0 & 0 \\ 0 & 0 & 1 & 0 & 0 & 0 \\ 0 & 0 & -\frac{tan(\varphi)}{R} & 1 & 0 & 0 \\ 0 & 0 & 0 & 0 & 1 & 0 \\ 0 & 0 & 0 & 0 & 0 & 1 \end{pmatrix}$$

R is the bending radius,
$\frac{s}{r}$ corresponds to the curvature angle,
γ is the relativistic gamma parameter and
φ is the angle of entering.
A sequence of an undulator period is described by:

$$\begin{aligned} M_{\lambda/4}(\Phi) &= R_{edge2} \cdot R_{sbend}(\Phi) \cdot R_{edge1}, \\ M_{period} &= M_{\lambda/4}(\Phi) \cdot M_{\lambda/4}(-\Phi) \cdot M_{\lambda/4}(-\Phi) \cdot M_{\lambda/4}(\Phi). \end{aligned}$$

The different signs in $R(+/-)$ characterises the different bending directions.

Elliptical Undulator

The field configuration of an elliptical undulator forces the electrons on helical trajectories. Dispersion tends to couple the motion in all three dimensions. Similar to the approach of planar undulator, the elliptical undulators will be split into a series of alternating Rbends. In contrast to the 'regular' bends of planar undulators the body of the Rbend-matrix consists of two bending planes. Thus, the Sbend-part is defined by:

$$(2.8)$$

$$\begin{pmatrix} cos(\frac{s}{R_1}) & R_1sin(\frac{s}{R_1}) & 0 & 0 & 0 & R_1(1-cos(\frac{s}{R_1})) \\ \frac{-1}{R_1}sin(\frac{s}{R_1}) & cos(\frac{s}{R_1}) & 0 & 0 & 0 & sin(\frac{s}{R_1}) \\ 0 & 0 & cos(\frac{s}{R_2}) & R_2sin(\frac{s}{R_2}) & 0 & R_2(1-cos(\frac{s}{R_2})) \\ 0 & 0 & \frac{-1}{R_2}sin(\frac{s}{R_2}) & cos(\frac{s}{R_2}) & 0 & sin(\frac{s}{R_2}) \\ -sin(\frac{s}{R_1}) & -R_1(1-cos(\frac{s}{R_1})) & -sin(\frac{s}{R_2}) & -R_2(1-cos(\frac{s}{R_2})) & 1 & R_{56} \\ 0 & 0 & 0 & 0 & 0 & 1 \end{pmatrix},$$

$$\text{with } R_{56} = -\sqrt{((R_1 \cdot sin(s/R_1) - s)^2 + (R_2 \cdot sin(s/R_2) - s)^2)} + \frac{s}{\gamma^2}.$$

The same goes to the matrix of edges.

$$
\begin{pmatrix}
1 & & 0 & 0 & & 0 & 0 & 0 \\
+\frac{tan(\varphi_1)}{R_1} - \frac{tan(\varphi_2)}{R_2} & & 1 & 0 & & 0 & 0 & 0 \\
0 & & 0 & 1 & & 0 & 0 & 0 \\
0 & & 0 & -\frac{tan(\varphi_1)}{R_1} + \frac{tan(\varphi_2)}{R_2} & 1 & 0 & 0 \\
0 & & 0 & 0 & & 0 & 1 & 0 \\
0 & & 0 & 0 & & 0 & 0 & 1
\end{pmatrix}, \tag{2.9}
$$

R_i is the curvature radius for each plane,
s is the pathlength along the trajectory,
$\frac{s}{R_i}$ corresponds to the bending angle and
γ is the relativistic gamma parameter.
The approach is based on a separated treatment of the bending for each plane. It is a superposition of two Rbends merged into one transfermatrix. The motion in both planes are assumed to be independent, only the element R_{56} depends on both motions simultaneously. The element R_{56} splits up into two parts. $\frac{s}{\gamma^2}$ describes the longitudinal displacement based on the relativistic dilatation. The other part manages the longitudinal displacement, which appears , if a beam is bended. It describes the additional pathlength $\Delta s = \sqrt{(\Delta x)^2 + (\Delta y)^2}$. The second matrix is the fusion of the edge focusing matrices for both transversal planes. A focusing effect of an edge in one plane is escorted from a defocusing effect in the other one. In the case of a superposition of two edges the focusing and defocusing effects in each plane will be overlaid, which leads to an effective (de-)focusing values. This algorithm offers the potential to cope with most kinds of undulators, regardless of their polarisations. Note that, this is an 1D-approximation. For complex field distributions the approximation is only valid in a small region around the undulator axis.

Genesis1.3 Undulator

Another approximation of undulator focusing is used in the FEL code Genesis1.3. In Genesis1.3 the impact of undulators on trajectories is approximated by a focusing strength(k_{undu}). The focusing strength is a function of undulator parameters as well as particle characteristics:

$$
k_{undu} = \left(\frac{2\pi \cdot xkx \cdot K_{rms}}{\lambda_u \gamma} \right)^2. \tag{2.10}
$$

Undulator parameters are undulator period λ_u, undulator parameter K_{rms} and $xkx \, \epsilon \, [0, 1]$, which characterises different kinds of undulator types. The undulator parameter K_{rms} stands for the amplitude of the electron momentum oscillation. In the case of a planar undulator the focusing plane is described similar to the focusing plane of quadrupoles. In the other plane the undulator acts almost like a

drift. Genesis1.3 uses the equations of motion for the single particles, which are:

$$
\begin{aligned}
\varphi_u &= \sqrt{|k_{undu}|} \cdot s, \\
x(s) &= cos(\varphi_u) \cdot x_0 + \frac{1}{\sqrt{|k_{undu}|}} sin(\varphi_u) \cdot x_0', \\
x'(s) &= -\sqrt{|k_{undu}|} sin(\varphi_u) \cdot x_0 + cos(\varphi_u) \cdot x_0', \\
y(s) &= y_0 + s \cdot y_0', \\
y'(s) &= y_0'.
\end{aligned}
$$

Undulator with End Pole

A special feature of every undulator is the 'endpoles' [13]. Two periods are used to centre the oscillating motion of the beam inside the undulator. While the beam enters the undulator, it passes the first half period of endpoles, whose integrated field strength amounts to a quarter of the main undulator strength. In the second half period the integrated field strength increases to three-quarter of the main undulator strength. Due to the resulting displacement the oscillation takes place at the centred axis of the undulator. The second period of endpoles locates at the end of the undulator. It cancels the displacement of the first endpoles at the beginning of the undulator. Due to the second endpoles the beam is centred in the beam pipe again. The endpoles split up to two different integrated field strengths. The configuration can be achieved by a combination of a lower field strength with
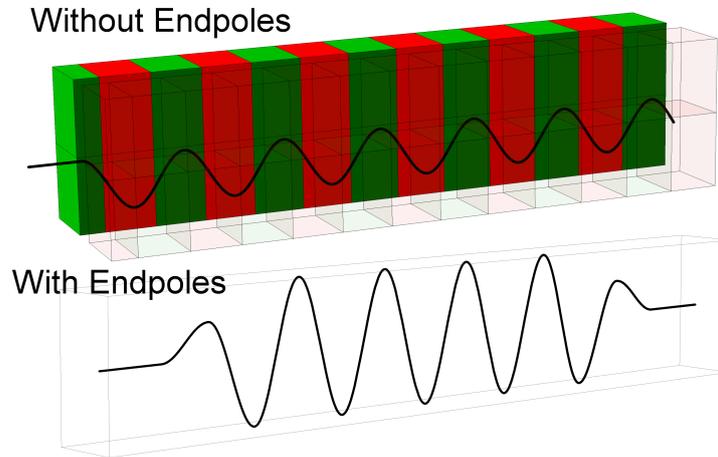
Figure 2.3:   Impact of Endpoles
Due to the endpoles the oscillating motion of the beam is centred at the undulator axes.

the same period length or by a shorter period length with the same field strength. Lower field-strength arrangements are often used for permanent magnetic devices. In the case of electrodynamic magnetic structures shorter period lengths are very popular. This is based on magnetic characteristics, like hysteresis.

2.3 Space Charge

The interaction of charged particles with each other and their environment via electro-magnetic fields, is the subject of this section. A general introduction, describing the fundamental concepts and assumptions regarding electro-magnetic fields and space charge effects in accelerators, is given in the first part of this section. Later then, the space charge effects as an impact of charged particle distributions acting on themselves will be discussed.

2.3.1 Fundamentals

The force experienced by a charged particle, which is influenced by electro-magnetic fields, is given by the Lorentz-force:

$$\vec{F} = q(\vec{E} + \vec{v} \times \vec{B}). \tag{2.11}$$

A resting charged particle itself is a source of an electric field and if the particle moves, it becomes a source of an additional magnetic field. The relation between charges, currents, electric fields and magnetic fields is given by the following Maxwell equations [14]:

$$
\begin{aligned}
\nabla \cdot \vec{E} &= \frac{\varrho}{\epsilon_0}, \\
\nabla \times \vec{E} &= -\frac{\partial \vec{B}}{\partial t}, \\
\nabla \cdot \vec{B} &= 0, \\
\nabla \times \vec{B} &= \mu_0 \vec{j} + \frac{1}{c^2} \frac{\partial \vec{E}}{\partial t}.
\end{aligned}
\tag{2.12}
$$

The relation between the scalar potential Φ of an electric field and its source, the charge distribution, is given by:

$$
\begin{aligned}
\nabla^2 \Phi &= \frac{\varrho}{\epsilon_0} \quad \text{with} \\
\vec{E} &= -\nabla \Phi.
\end{aligned}
\tag{2.13}
$$

$\Phi(\vec{r})$ is a scalar potential, which describes the potential energy of charged particles. The magnetic analogon to Φ is the vector potential $\vec{A}(\vec{r})$. It is described by:

$$
\begin{aligned}
\vec{A}(\vec{x}) &= \frac{\mu_0}{4\pi} \int \frac{\vec{j}(\vec{x}')}{|\vec{x}' - \vec{x}|} \mathrm{d}^3 x' \\
\vec{B} &= \nabla \times \vec{A}.
\end{aligned}
\tag{2.14}
$$
$$
\tag{2.15}
$$

Self-Fields

From electrostatics it is known, that two resting charged particles with the same sign of charge reject each other. So they split off with the force:

$$\vec{F} = \frac{q_a q_b}{4\pi\epsilon_0 r_{ab}}\vec{e_r}. \tag{2.16}$$

The acting force depends linearly on the charges of both particles, q_a and q_b, and decreases with their distance r_{ab}. In the case of a moving particle, the situation changes.
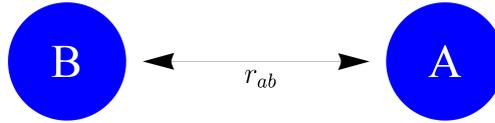
Figure 2.4: Space Charge in Electrostatic Case
The force between two resting charged particles is defined by eq. 2.16.
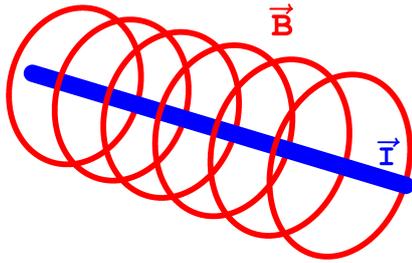
Figure 2.5: Magnetic Field

Moving charges present a current I. Each current generates a magnetic field B. In steady state, i.e. when the current density does not change neither its direction nor its magnitude, the Biot-Savart-law gives the resulting magnetic field:

The magnetic field is concentric to the current.

$$\vec{B}(\vec{r}) = \frac{\mu_0}{4\pi}\nabla \times \int \frac{\vec{j}(\vec{r'})}{|\vec{r}-\vec{r'}|}\mathrm{d}^3 r'. \tag{2.17}$$

In contrast to the repulsive effect of the electric field, the magnetic field induces an attractive force. For relativistic particles the equivalence of the electrostatic case in the centre of mass system (cms) and the electrodynamics in the laboratory-system, becomes obvious. In other words, according to

$$F(v) = F(0) \cdot (1 - \beta^2) \quad \text{with } \beta = \frac{v}{c}$$

the force decreases, while the velocity increases, and vanishes for $v \to c$. If particles move with c (parallel and in same direction), the time in cms slow down due to time dilatation, as shown left [15].
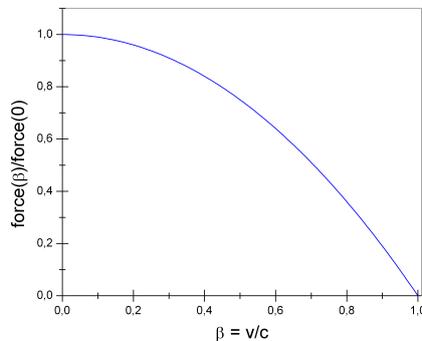
Figure 2.6: Impact of Velocity

The Environment

The interaction of charged particles with their environment is another aspect of the space charge effects.
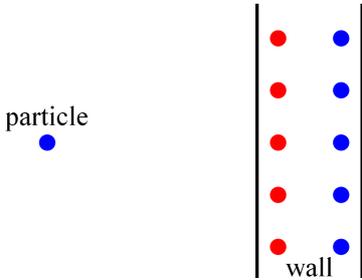
Figure 2.7: Particle-Wall-Interaction
The particle induces a charge separation inside the wall.

A classical example, applicable on charged particles in a vacuum chamber, is plotted left hand side. The charged particle rests near a wall ($\Phi_{wall} = 0$). Assuming, the wall is expanded to infinity. Instead of coping with a single charge and a wall, the wall can be replace by image charges. The combination of charges and image charges has to meet the boundary condition ($\Phi_{wall} = 0$). The wall position is $\vec{r}_{wall} = (0,0)$ and the particle locates at $\vec{r}_{original} = (-x,0)$.

For supplying the boundary condition an image charge with the same charge value but opposite sign of charge is positioned at $\vec{r}_{image} = (x,0)$. Hence, the acting force can be calculated according to eq. 2.16. The wall-electron-interaction is of particular interest in an accelerator, as a bunch of charged particles, e.g. electrons, interacts with the chamber wall.

A simple model is an ensemble of charged particles in a conducting pipe, whereby a slowly varying longitudinal bunch profile is assumed. The longitudinal dimension of the bunch is huge compared to the transversal ones. On condition of neglected retardation effect it simplifies to a two dimensional electrostatic problem. A detailed development is presented in [14]. In a more careful treatment of this interaction, further aspects, like the electric conductivity of the pipe, pipe profile, retarding effects and repetition rate, have to be taken into account. It is called 'wake-fields'. The issue of wake-fields is discussed in details in many publications, e.g. [15],[16].
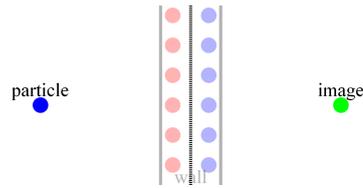
Figure 2.8: Image Charge
The wall can be replaced by image charges.
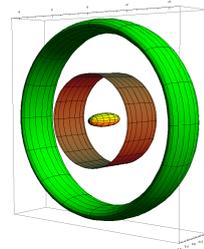
Figure 2.9: Bunch in Pipe
In this 3d case an image charge density is required.

Relativistic Effects

Two major different regimes depending on the particle velocity take place in the investigation of space charge effects. For non-relativistic particles (first regime) retarding effects can be neglected. The field calculation follows directly from the

charge distribution. For complex charge distributions an analytical solution can be approached by harmonic expansion.

For relativistic particles (second regime) the retarding effects have to be taken into account. Every charge distribution creates electro-magnetic fields, which act back on the distribution itself. Thus, for a solution both, field and distribution, have to be considered simultaneously. The solution has to be self-consistent.

2.3.2 Charge Distribution Models and Space Charge Effects

Simulation codes, like ASTRA, calculate space charge impact in a self-consistent manner by particle tracking. Unfortunately, those simulations require a lot of CPU-time. For a fast pre-calculation some assumptions and approximations have to be made, which are described in the following.

The pre-calculation of self-fields is connected with well chosen assumptions about charge distribution in a well defined integration volume. In such models the symmetry of the charge distribution often determines the boundary condition of the integration. An example is the triaxial ellipsoid with uniform or three dimensional gaussian charge distribution. Lapostolle discussed this model in [17]. In the present work transversal models are discussed, which are similar to the known three dimensional, triaxial ellipsoid model. The development of the field distribution of the three dimensional ellipsoid with uniform charge distribution is presented in [18]. A short description is also given in appendix C. In the limit of a small transverse cross section (compared to the longitudinal dimension), the 3 dimensional ellipsoid can be seen as a series of such similar transversal models. This limit is satisfied in multi-cascade FELs.

Model of Uniform Charge Distribution

The field calculation starts with the Maxwell eq.s (2.12). In the case of an uniform charge distribution, i.e. the distribution is uniform and homogeneous in all three dimension, the charge density ϱ_0 is extractable from the integrals:

$$\iiint\limits_{ellipsoid} \frac{\varrho(\vec{r})}{\epsilon_0} \mathrm{d}^3\mathrm{r} \;=\; \iint\limits_{surface} \vec{E} \cdot \mathrm{d}\vec{A}, \tag{2.18}$$

$$\iint\limits_{cross\ section} \mu_0 |\vec{j}| \vec{e}_{\vec{v}} \cdot \mathrm{d}\vec{A} \;=\; \oint\limits_{circumference} \vec{B} \cdot \mathrm{d}\vec{s}, \tag{2.19}$$

$$\text{with } \vec{j}(\vec{r}) \;=\; \varrho(\vec{r}) \cdot c \cdot \vec{\beta}. \tag{2.20}$$

The charge density as well as the current density inside the ellipsoid determine the field distribution on the surface (eq. 2.18 and 2.19). The integration limits

relate on border of the ellipsoid. For HGHG-FEL the bunch profile is approached by a cylinder. In eq. 2.18 the volume integration transforms into integration over the lateral surface. It is:

$$\iint\limits_{surface} \vec{K} \cdot \mathrm{d}\vec{A} = \int\limits_0^{l_o} \oint\limits_C \vec{K} \cdot \vec{n} \ \mathrm{d}u\mathrm{d}l, \tag{2.21}$$

$$\text{where } C \text{ is the circumference.}$$

$\vec{K}$ stands for any vector field. $\vec{n}$ marks the surface normal vector.
Unfortunately, there is no analytical expression for the circumference of an ellipse. If the relation of the semi axis (a, b) is known, the circumference ascertains by numerical elliptical integrals. An approach for circumferences of ellipses is given in [19]:

$$u = \pi(a+b) \cdot [1 + \frac{\lambda^2}{4} + \frac{\lambda^4}{64} + \cdots], \tag{2.22}$$

$$\text{with } \lambda = \frac{a-b}{a+b}. \tag{2.23}$$

As shown in [18], it is possible to avoid this 'problem' by a special coordinate transformation (in 3D). Instead of using the more in common elliptical coordinates, the coordinates are expressed as a combination of zeros of the profile function, eq. 2.24, and the dimensions of the semi axes (a, b, c):

$$f(s) = \frac{x^2}{a^2+s} + \frac{y^2}{b^2+s} + \frac{z^2}{c^2+s} - 1, \tag{2.24}$$

$$\varphi(s) = (a^2+s)(b^2+s)(c^2+s). \tag{2.25}$$

This simplifies the determination of the electric fields to a one-dimensional integration:

$$E_x = 2\pi abc\varrho_0 x \int\limits_0^{\infty} \frac{\mathrm{d}s}{(a^2+s)\sqrt{\varphi(s)}}. \tag{2.26}$$

The other electric fields in y- and z- direction calculate similar to E_x by replacing a by b and c inside the integral of eq. 2.26 as well as x by y and z. Those electric fields relate to a triaxial ellipsoid with uniform charge distribution in its centre of mass system.
A two dimensional model of this approach can also be based on the assumption of an uniform charge distribution. The longitudinal axis of the triaxial ellipsoid increases to infinity, thus $c \gg a, b$. Any dependency of c in eq. 2.26 vanishes. The triaxial ellipsoid becomes a continuous beam with constant current and an
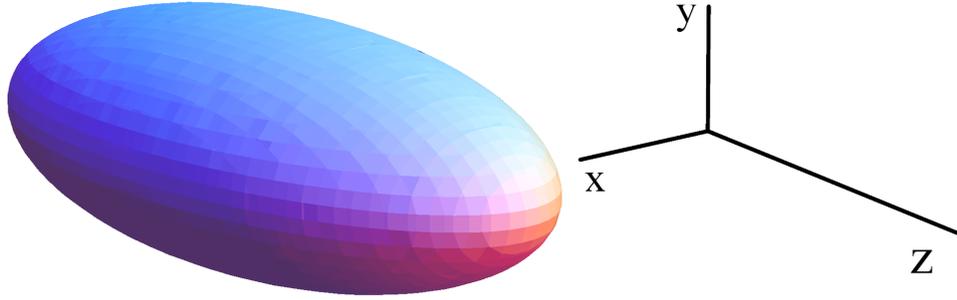
Figure 2.10:   Model of a Triaxial Ellipsoid

The triaxial ellipsoid is characterised by three different semi axes. Therefore, the profile of the ellipsoid can be similar to the profile of a zeppelin.

elliptical cross section. In this limit the profile function as well as $\varphi(s)$ simplifies to:

$$f_{2D}(s) = \frac{x^2}{a^2 + s} + \frac{y^2}{b^2 + s} - 1, \tag{2.27}$$

$$\varphi_{2D}(s) = (a^2 + s)(b^2 + s). \tag{2.28}$$

A similar coordinate transformation yields the expression for the coordinates:

$$x^2 = \frac{(a^2 + \lambda)(a^2 + \mu)}{a^2 - b^2}, \tag{2.29}$$

$$y^2 = \frac{(b^2 + \lambda)(b^2 + \mu)}{b^2 - a^2}. \tag{2.30}$$

λ and μ represent the zeros for the 'new' profile function eq. 2.27. Due to the limit of the longitudinal dimension, $c \to \infty$, the charge density and the longitudinal dimension in eq. 2.26 will be replaced by an average current I and the particle velocity v. The distribution function $n(x, y)$ along the cross section was already extracted:

$$E_x = \frac{I}{2\epsilon_0 v} abx \int_0^\infty \frac{n \ ds}{(a^2 + s)\sqrt{\varphi(s)}}. \tag{2.31}$$

Different charge distributions inside the cross section, i.e. integration surface, are discussed in [20]. In the case of an uniform distribution the function $n(x, y)$ becomes a constant and can be extracted form the integral:

$$n(x, y) = \frac{1}{\pi ab}. \tag{2.32}$$

The integral becomes:

$$E_x = \frac{I}{2\pi\epsilon_0 v} x \int\limits_0^\infty \frac{\mathrm{d}s}{(a^2 + s)^{\frac{3}{2}}\sqrt{(b^2 + s)}}. \tag{2.33}$$

From this the expressions of the electric fields in x- and y-direction follow:

$$E_x = \frac{I}{\pi\epsilon_0 v} \frac{x}{(a + b)a}, \tag{2.34}$$

$$E_y = \frac{I}{\pi\epsilon_0 v} \frac{y}{(a + b)b}. \tag{2.35}$$

These fields corresponds to the particle ensemble in its centre of mass system. The impact of the particle velocity causes a counteracting magnetic field. The transformation from the centre of mass frame to the laboratory frame leads to an additional factor $\frac{1}{\gamma^2}$. As a conclusion of eq. 2.34 and eq. 2.35 the resulting force on a particle with the charge e in the laboratory system becomes:

$$\vec{F}_{sc} = \frac{eI}{\beta c\epsilon_0\pi(a + b)\gamma^2} \begin{pmatrix} \frac{x}{a} \\ \frac{y}{b} \\ 0 \end{pmatrix}. \tag{2.36}$$

A important characteristic is, that the magnitude of the resulting force is a function of the particle energy. Furthermore, there are no correlations between different planes. In each transversal plane the resulting space charge force linearly depends on the particle position. That means, that particles near the border experience another magnitude of force than particles resting close to the centre of the cross section. Due to the space charge effects, any uniform charge distribution becomes inhomogeneous. In the following subsection, the requirements for a discussion of space charge impacts on non-homogeneous charge distributions will be shown. In order to simplify the discussion, a circular symmetrical bunch cross section is assumed.

Circular Symmetrical Cross Section & Uniform Charge Distribution
The calculation is performed in laboratory system. The additional factor $\frac{1}{\gamma^2}$ is expected from the combined impacts of the electrostatic fields and the magnetic fields on charged particles. The impact of different charge distributions is discussed for the special case of a circular transverse cross section, radius $= a$. Due to its symmetry the fields can be calculated directly from eq. 2.18. The electric field is parallel to the normal vector. Thus, the electric-field projection in eq. 2.18 is identical with the exact field configuration. The same applies to the magnetic field. In this model the particle propagation vector is defined by:

$$\vec{\beta}c \approx \vec{v}_s, \tag{2.37}$$

where s characterises the direction along the design path.

The eq.s 2.18 and 2.19 simplify to:

$$\frac{\varrho_0}{\epsilon_0} \iiint\limits_{cylinder} \mathrm{d}^3\mathrm{r} \;\; = \;\; E_r \iint\limits_{surface} \mathrm{d}A, \tag{2.38}$$

$$\mu_0 |\vec{j}| \iint\limits_{cross\ section} \mathrm{d}A \;\; = \;\; B_\varphi \oint\limits_C \mathrm{d}s, \tag{2.39}$$

where c is the circumference of the cross section. The charge distribution and current density will be expressed by the average current I. It is:

$$I = \int j \mathrm{d}A = \int \varrho \beta c \mathrm{d}A. \tag{2.40}$$

The resulting fields are :

$$E_r \;\; = \;\; \frac{I}{2\pi a^2 \epsilon_0 \beta c} r, \tag{2.41}$$

$$B_\varphi \;\; = \;\; \frac{\mu_0 I}{2\pi a^2} r, \tag{2.42}$$

where r is the particle position.

The transverse force is given by a combination of eq. 2.11 and eq. 2.37.

$$
\begin{aligned}
\vec{F}_{sc} \;\; &= \;\; e \cdot (\vec{E} + c \cdot \vec{\beta} \times \vec{B}) \\
&= \;\; eE(1 - \beta^2)\vec{e_r} \\
&= \;\; \frac{eI}{\beta c \epsilon_0 2\pi a^2 \, \gamma^2} \begin{pmatrix} x \\ y \\ 0 \end{pmatrix}.
\end{aligned}
\tag{2.43}
$$

Gaussian Charge Distribution

In contrast to the uniform distribution the gaussian distribution is even more realistic in storage rings, but it does not seem to be an exact model. At the tails of the distribution realistic bunches often show a halo. That means, the charge distribution does not vanish so rapidly as in the gaussian case. The calculation of the gaussian distribution is performed in the same manner as in the case of the uniform distribution. By assuming the rotational symmetry, the charge distribution is defined by:

$$\varrho(r) \;\; = \;\; \frac{I}{\beta c 2\pi \sigma^2} e^{-\frac{r^2}{2\sigma^2}}. \tag{2.44}$$

The resulting fields are marked by nonlinear characteristics:

$$\vec{E} \;\; = \;\; \frac{I}{\beta c 2\pi \epsilon_0} \frac{1}{r} (1 - e^{-\frac{r^2}{2\sigma^2}}) \cdot \vec{e}_r, \tag{2.45}$$

$$\vec{B} \quad = \quad \frac{I}{c^2 2\pi\epsilon_0} \frac{1}{r}(1 - e^{-\frac{r^2}{2\sigma^2}}) \cdot \vec{e}_\varphi. \qquad (2.46)$$

The space charge force results to:

$$\vec{F} \quad = \quad \frac{eI}{\beta c 2\pi\epsilon_0 \gamma^2} \frac{1}{r}(1 - e^{-\frac{r^2}{2\sigma^2}}) \cdot \vec{e}_r. \qquad (2.47)$$

In contrast to the uniform distribution, the gaussian distribution is characterised by a nonlinear behaviour. Although only a homogeneous charge distribution creates self-fields with a linear dependency on the coordinates, one can assume a linear dependency in the core region for gaussian distributions as well. A linear approach for the gaussian space charge force corresponds to the calculated force till about 0.8 σ.
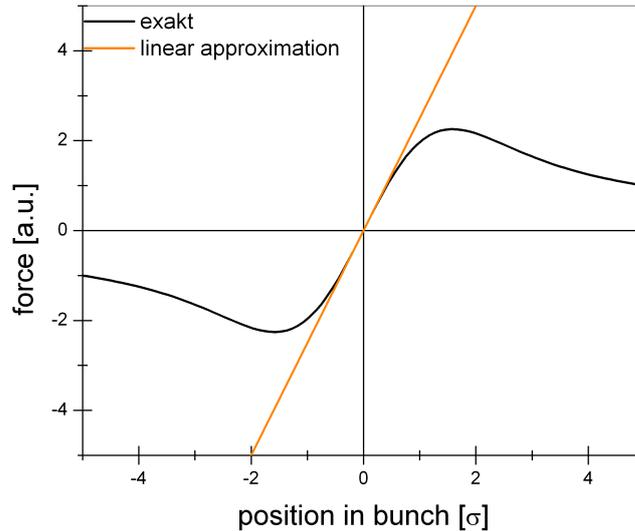
Figure 2.11:   Space Charge Force of Gaussian Distribution and the Linear Approximation

This plot shows the force, produced by space charge effects of a gaussian charge distributions versus the particle position. The linear approach fits the exact force in the range of -0.8σ to 0.8σ.

Generally, it is accepted that the linear part of any internal and external forces dominates the development of the second moments of a distribution. Beyond that, the actual distribution seems to be less important than the RMS-values. The development of the second moments (RMS/envelope) of different distribution is very similar. This leads to the development of an 'equivalent uniform beam' model [21],[16], which can be used for pre-calculation of a realistic beam

distribution. The second moments of the equivalent uniform beam correspond to the second moments of the exact charge distribution. The second moments of several distributions can be found in app. B. The equation 2.24 determines the profile of the equivalent uniform beam in three dimensions, and the equation 2.27 in two dimensions. The semi-axes are defined as:

$$
\begin{aligned}
a &= \sigma_x \cdot \sqrt{5}, \\
b &= \sigma_y \cdot \sqrt{5}, \\
c &= \sigma_z \cdot \sqrt{5}.
\end{aligned}
$$

σ_i are the RMS-values, which are given by the exact charge distribution.
So far, a very long bunch was assumed. In this case the impact of the longitudinal dimension as well as longitudinal self-fields are neglected. If the bunch becomes short and the longitudinal dimension of the bunch reaches the same magnitude as the dimension of the cross section, the bunch profile becomes crucial.
The 'Space Charge Form Factor' f modifies the values of the self-fields in each direction. It is determined by the ratio of the bunch length and the dimension of the cross section.
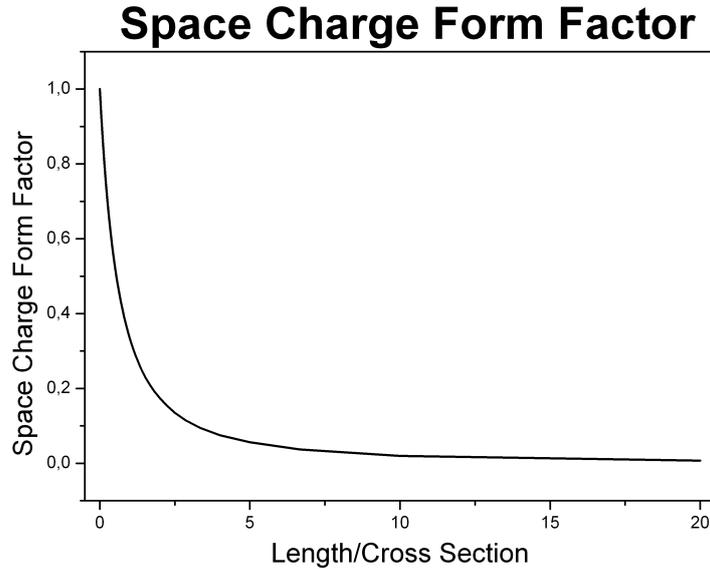
Figure 2.12:   Space Charge Form Factor

The space charge form factor describes the impact of the bunch profile on the space charge fields. A criterion is the ratio of the bunch length and the dimensions of the bunch cross section.

The longitudinal space-charge field linearly depends on the space-charge form-factor f, whereas the transversal fields linearly depend on $(1 - f)$ [22]. Lapostolle

also pronounced these modifications of the field strengths [17]. The counter part of a continuous beam is an infinitesimal long beam or even more a disc. In this case the impact of the transversal space-charge fields vanishes. The impact of the longitudinal space-charge fields become maximal. Note that, the effects of the longitudinal space charge are beyond the scope of the present work, as the space charge form factor in HGHG-Structures tends to zero:

$$x = \frac{r_z \gamma}{\sqrt{r_x r_y}},$$

$$e.g. \ x = \frac{1ps \cdot 3 \ 10^{+8}\frac{m}{s} \cdot 2348.34}{100\mu m} \approx 7045 \Rightarrow f(x) = 0.$$

2.4 Space Charge Implementation

The calculation of beam optics in accelerator physics is executed in a particular way. The development in time is transformed into a development along the trajectory. Thus, the impacts of space charge effects have to be transformed as well. The eq.s 2.34 and 2.35 determine the space-charge field distributions of the equivalent beam model in the centre of mass system. The transformation of the resulting space charge force into an expression, which is more common in accelerator physics, yields:

$$F = m\ddot{r} = m\frac{\mathrm{d}^2}{\mathrm{d}t^2}r,$$

$$= m_0 \gamma \beta^2 c^2 \ r''. \tag{2.48}$$

A separated treatment for each plane is possible, where the space charge force points in the direction of the projected displacement x:

$$x'' = \frac{F_x}{m_0 \gamma \ \beta^2 c^2},$$

$$x'' = k_{sc} \ x. \tag{2.49}$$

This formula is identical with the equation of motion in the defocusing plane of quadrupoles, see app. A. The coefficient k_{sc} describes the defocusing strength of the space charge effect. Due to the space charge effects the equations of motions in the accelerator elements change. The additional defocusing effects have to be included. This leads to modified transfermatrices as described below. Note, that longitudinal space charge effects are neglected.

Drift

In drift sections, where any external forces are neglected, the equations of motion are given by eq. 2.49. Thus, the space charge defocusing in drifts can be expressed by a modified duplex defocusing matrix, whereas the defocusing strength in each plane is given by the space-charge defocusing strengths. The transfermatrix of drifts transforms to:

$$
\begin{pmatrix}
cosh(\sqrt{|k_{sc_x}|}s) & \frac{1}{\sqrt{|k_{sc_x}|}}sinh(\sqrt{|k_{sc_x}|}s) & 0 & 0 & 0 & 0 \\
\sqrt{|k_{sc_x}|}sinh(\sqrt{|k_{sc_x}|}s) & cosh(\sqrt{|k_{sc_x}|}s) & 0 & 0 & 0 & 0 \\
0 & 0 & cosh(\sqrt{|k_{sc_y}|}s) & \frac{1}{\sqrt{|k_{sc_y}|}}sinh(\sqrt{|k_{sc_y}|}s) & 0 & 0 \\
0 & 0 & \sqrt{|k_{sc_y}|}sinh(\sqrt{|k_{sc_y}|}s) & cosh(\sqrt{|k_{sc_y}|}s) & 0 & 0 \\
0 & 0 & 0 & 0 & 1 & \frac{s}{\gamma^2} \\
0 & 0 & 0 & 0 & 0 & 1
\end{pmatrix}.
$$

Quadrupole

Quadrupoles are characterised by their focusing features. Due to the space charge effects the equations of motion for quadrupoles change to:

$$
\begin{aligned}
x'' + (k_{qp_x} - k_{sc_x})x &= 0, \\
y'' - (k_{qp_y} + k_{sc_y})y &= 0.
\end{aligned}
$$

In the defocusing plane of quadrupoles the defocusing strength increases to the sum of both defocusing strengths. The quadrupole focusing strength decreases due to the impact of the space-charge defocusing strength. In this case three different regimes have to be distinguished. If the space charge defocusing is weaker than the focusing of the quadrupole, the resulting effect remains focusing. If the space charge defocusing is stronger than the focusing of the quadrupole, the resulting effect will be defocusing. In the case of an equilibrium between space charge defocusing and quadrupole focusing the quadrupole will act like a drift in the focusing plane. The transfermatrices for the different regimes can be easily calculated. In app. A the development of the transfermatrix elements for quadrupoles without the impact of space charge is given. This development yields the correct transfermatrices with space charge impacts by replacing the quadrupole strength k with an effective quadrupole strength $k_{eff} = \sum k_i$ and Δk_i.

Bend

From the eq.s 2.34 and 2.35 it follows, that the effect of transverse space charge in a linear approach is separable in the two transversal planes. Furthermore, the impact of the longitudinal space charge is also independent of the field distributions in the transverse plane. In consequence a simple implementation in existing programs seems to be possible. The focusing strength of all elements couples to the space charge defocusing. Unfortunately, this approach does not work in all

elements. The treatment of bends is more complicated. The equation of motion for particles in a bend (bending in x-z plane) is defined by:

$$x''(s) + (\frac{1}{R^2(s)} - k_{sc_x}(s))x(s) = \frac{1}{R(s)}\frac{\Delta p}{p}, \qquad (2.50)$$

$$y''(s) - k_{sc_y}(s)y(s) = 0. \qquad (2.51)$$

In the non-bending plane the bend acts like the defocusing plane of quadrupoles. In the bending plane, there is a coupling between the transverse and the longitudinal motion. If the energy deviation is not zero, i.e. $\frac{\Delta p}{p} \neq 0$, the dispersive effect takes place. The effect of the dispersion creates its own dynamics, which will be discussed in the next section. Furthermore, the physical characteristics of bending magnets leads to another effect, whereby even in the absence of dispersion a development of the equation of motion similar to quadrupoles is hard to manage. This will be discussed in the last part of this chapter.

2.4.1 Space Charge Effect and Dispersion Part I

Although fields of space charge separate and act in different planes, a coupling of those space charge fields could take place. In dispersive elements, like bends, a coupling between the longitudinal and transverse motion occurs. Therefore, the transverse space charge acts on the longitudinal dimensions of the bunch.

combined function approach

The following development is performed in analogy to the development of the regular dispersion elements, shown in app. A.
The equation of motion including space charge effects becomes:

$$x''(s) + (\frac{1}{R^2(s)} - k_{sc})x(s) = \frac{1}{R(s)}\frac{\Delta p}{p}. \qquad (2.52)$$

The impact of space charge is restricted to the focusing effect of the bend, if the energy spread vanishes, i.e. $\frac{\Delta p}{p} = 0$. This is realised for an ensemble of particles, where all particles have the same energy. In general this condition is not fulfilled. As a consequence the dispersive effect of the bend happens. In the following derivation a constant energy spread and a constant curvature radius are assumed. The combination of weak focusing and space charge contribution is replaced by the abbreviation:

$$k = \frac{1}{R^2} - k_{sc}. \qquad (2.53)$$

This definition of k is similar to the definition of the focusing strength of *combined-function* bending magnets [23] . The equation of dispersion becomes:

$$D''(s) + k\,D(s) = \frac{1}{R}. \qquad (2.54)$$

Hence it follows: for a bend-dominated focusing ($k > 0$),

$$R_{16} = \frac{1}{|k|\,R}(1 - cos(\sqrt{|k|}s)) \tag{2.55}$$

$$R_{26} = \frac{1}{\sqrt{|k|}\,R}sin(\sqrt{|k|}s). \tag{2.56}$$

In the case of a space-charge dominated focusing ($k < 0$), the elements change to

$$R_{16} = -\frac{1}{|k|\,R}(1 - cosh(\sqrt{|k|}s)) \tag{2.57}$$

$$R_{26} = \frac{1}{\sqrt{|k|}\,R}sinh(\sqrt{|k|}s). \tag{2.58}$$

This development is only correct, if the energy spread $\frac{\Delta p}{p}$ remains constant. The impact of longitudinal space charge is a change of the energy spread. Thus, in the case of including longitudinal space charge effects, the transfermatrix elements R_{15}, R_{25}, R_{61} and R_{62} of bends might not remain zero. The effect of the longitudinal space charge will also couple with the transversal motion.

space charge kick approach

In some simulation codes, e.g. Trace3D, the impact of space charge is implemented by 'space charge kicks'. The space charge defocusing is simulated by an element, which has no longitudinal extension. The effect of this elements is similar to the effect of the element *edge*. It changes the divergence of beams.
At several positions the beam divergence is modified by those kicks.

$$M_{kick}^{6\,dim.} = \begin{pmatrix} a_{11} & \ldots & a_{16} \\ \vdots & & \vdots \\ a_{61} & \ldots & a_{66} \end{pmatrix}$$

In the case of separated kicks in the transversal and longitudinal planes, this matrix decays to three sub-matrices. A calculation of a Sbend matrix with a defocusing space-charge kick demonstrates also a change of the dispersion elements:

$$R_{16}^* = R_{16}a_{11} + R_{26}a_{12},$$
$$R_{26}^* = R_{16}a_{21} + R_{26}a_{22}.$$

Assuming the thin lens formula for the sub-matrices, the dispersion elements transform to:

$$R_{16}^* = R_{16}, \tag{2.59}$$

$$R_{26}^* = R_{16}\frac{1}{f} + R_{26}. \tag{2.60}$$

Here, f characterises the focus of the space charge impact.

The new dispersion elements are marked by *. In contrast to eq. 2.57 the dispersion element R_{16} does not change. But, the element R_{26} becomes modified by the space charge. After a small drift this element causes a change of the element R_{16}. In the limit of an infinitesimal step size this approach will in theory be suitable. Similar to the coupling of longitudinal and transversal motion a coupling of the two transversal planes might lead to a similar discussion as well. Such a coupling occurs in elements like solenoids and skew quadrupoles.

2.4.2 Space Charge Effect and Dispersion Part II

The second specific characteristic of bends is illustrated in figure 2.13.
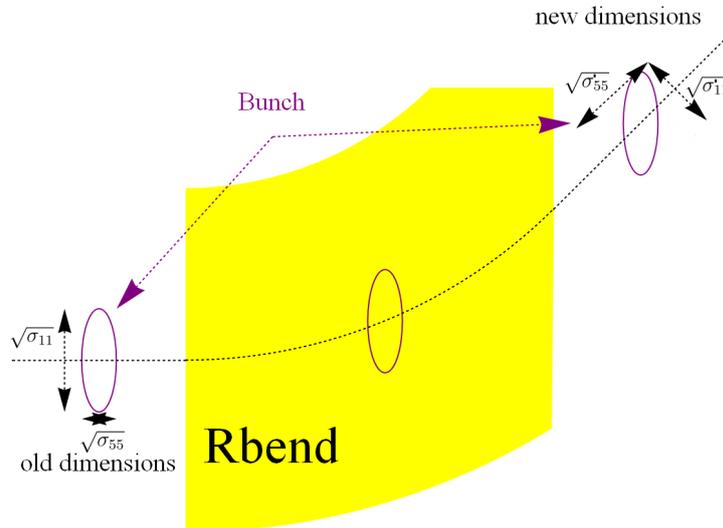
Figure 2.13:   Bunch in a Bend

If a bunch enters a bend, the bunch rotates in the reference system, while it does not rotate in the laboratory system.

The σ-matrix expresses the bunch extensions in the reference system by the square root of the diagonal elements, $\sigma_{11}, \ldots \sigma_{66}$ [24]. If the coupling elements σ_{13}, σ_{15} and σ_{35} are zero, the bunch is upright in the reference system. Thus, the bunch dimensions in the centre of mass system correspond to the bunch extensions in the reference system. If a bunch passes through a bend, the bunch rotates in the reference system. The resulting dimensions of the bunch and the rotation angle can be expressed by the σ-matrix. In this case at least one of the coupling elements is not zero. The σ-matrix has to be transformed into a matrix with vanishing coupling elements, as the equations of space charge fields relate to an ellipsoid in the centre of mass system. The elements σ_{11}, σ_{33} and σ_{55} of this

transformed σ-matrix contain the correct dimensions for the space charge formula. Nevertheless, those space charge fields are expressed in the cms-system of the bunch. In return the defocusing strengths must be transformed into the reference system. In the case of bends this transformation leads to a combined defocusing strength, which contains transversal and longitudinal defocusing contributions. The following calculation scheme cuts it into short.

The simplified σ-matrix contains only the bunch dimensions.

$$
\begin{pmatrix} \sigma_{11} & \sigma_{12} & \sigma_{13} \\ \sigma_{21} & \sigma_{22} & \sigma_{23} \\ \sigma_{31} & \sigma_{32} & \sigma_{55} \end{pmatrix} \Rightarrow \begin{pmatrix} a & 0 & 0 \\ 0 & b & 0 \\ 0 & 0 & c \end{pmatrix}
$$

From this matrix the bunch dimensions are taken to calculate the space charge fields and the defocusing strengths k_i. They are expressed in the diagonal matrix, which has to be transformed back by the transformation algorithm used above in reverse direction.

$$
\begin{pmatrix} k_x & 0 & 0 \\ 0 & k_y & 0 \\ 0 & 0 & k_z \end{pmatrix} \Rightarrow \begin{pmatrix} \kappa_{11} & \kappa_{12} & \kappa_{13} \\ \kappa_{21} & \kappa_{22} & \kappa_{23} \\ \kappa_{31} & \kappa_{32} & \kappa_{33} \end{pmatrix}
$$

This matrix describes the developed space-charge defocusing in the reference system. From this point it seems to be easy to cope with space charge effects in bends. The impact of the transversal space-charge effects is an additional defocusing. But the impact of the longitudinal space charge effects is a change of the energy spread. In a linear approach the change of the energy spread will be also a function of the particle position. The change of the energy spread cause a change of the coupling between the transverse and the longitudinal motion. Thus, additional correlation elements between transversal and longitudinal coordinates will be created. Sbend (bending in x-z plane) matrix without longitudinal space charge effects is defined by:

$$
R_{without\ l.SC} = \begin{pmatrix} R_{11} & R_{12} & 0 & 0 & 0 & R_{16} \\ R_{21} & R_{22} & 0 & 0 & 0 & R_{26} \\ 0 & 0 & R_{33} & R_{34} & 0 & 0 \\ 0 & 0 & R_{43} & R_{44} & 0 & 0 \\ R_{51} & R_{52} & 0 & 0 & 1 & R_{56} \\ 0 & 0 & 0 & 0 & 0 & 1 \end{pmatrix}.
$$

Sbend matrix with longitudinal space charge effects becomes:

$$
R_{with\ l.SC} = \begin{pmatrix} R_{11} & R_{12} & 0 & 0 & R_{15} & R_{16} \\ R_{21} & R_{22} & 0 & 0 & R_{25} & R_{26} \\ 0 & 0 & R_{33} & R_{34} & 0 & 0 \\ 0 & 0 & R_{43} & R_{44} & 0 & 0 \\ R_{51} & R_{52} & 0 & 0 & R_{55} & R_{56} \\ R_{61} & R_{62} & 0 & 0 & R_{65} & R_{66} \end{pmatrix}.
$$

The bunch dimensions in the bending plane as well as the transversal divergence and the energy spread are completely coupled.

3

The Program

Generally, simulation programs are limited by their initial assumptions and approximations, which are necessary for the calculations. An efficient employment of a program is achieved, if the task is adapted to the skills of the program. The aim of creating P12 was the need of a fast calculating tool for beam optics. P12 is suitable for lattice design without space charge effects, for the investigation of space charge impacts on beam optics and in a combined employment with other space-charge calculating programs, P12 can also be used as a diagnostic tool.

Due to the development of the bunch properties during the passage through the accelerator the space charge effects changes. For the calculation of the impact of space charge effects on optics, it is crucial to update the space charge force during the passage through a lattice. This demands the fragmentation of all used elements, which is discussed in the first part of this chapter. The second part deals with input parameters, special features and further assumptions included in the code of P12.

3.1   Fragmentation of Elements

A requirement of space charge calculations is the knowledge of the instantaneous bunch properties. This requires an updating of the transfermatrices and the fragmentation of the beam optics elements. Most of the elements involved in P12 are easy to split up.

Drift

In the drift matrix the elements depend linearly on the drift length. The result of the multiplication of two drift transfermatrices corresponds to the transfermatrix of a drift, whose driftlength is equal to the sum of both driftlengths.

$$\begin{pmatrix} 1 & L_1 \\ 0 & 1 \end{pmatrix} \begin{pmatrix} 1 & L_2 \\ 0 & 1 \end{pmatrix} = \begin{pmatrix} 1 & L_1 + L_2 \\ 0 & 1 \end{pmatrix}$$

Sbend and Quadrupole

In the case of quadrupoles and Sbends the multiplication leads to a more complex finding. This is based on the focusing character of such elements. Nevertheless, these expressions can be transformed into a matrix construction, which is identical to the transfermatrix for an element with a length given as the sum of the lengths of both individual elements. This is also valid in the case of the dispersive elements

of bending magnets.

$$\begin{pmatrix} cos(\varphi_1) & \frac{1}{\sqrt{k}}sin(\varphi_1) \\ -\sqrt{k}sin(\varphi_1) & cos(\varphi_1) \end{pmatrix} \begin{pmatrix} cos(\varphi_2) & \frac{1}{\sqrt{k}}sin(\varphi_2) \\ -\sqrt{k}sin(\varphi_2) & cos(\varphi_2) \end{pmatrix} = \begin{pmatrix} cos(\varphi_1 + \varphi_2) & \frac{1}{\sqrt{k}}sin(\varphi_1 + \varphi_2) \\ -\sqrt{k}sin(\varphi_1 + \varphi_2) & cos(\varphi_1 + \varphi_2) \end{pmatrix}$$

A combination of two subsequent quadrupoles can be expressed as one quadrupole, whose length is the sum of both individual lengths. Hence it follows, a quadrupole can also be subdivided into several quadrupoles under the conservation of the total quadrupole length. This fragmentation is also valid for Sbends.

Rbend

For the space charge calculations in P12 the fragmentation of Rbends is considered as well. The treatment of Rbends requires the addition of a focusing kick, so called edge. The corresponding focusing elements have no longitudinal expansion, see app A. A fragmentation of Rbends is realized by a separated treatment of the constituent parts of Rbends. For edges, there is no need to split them off. The middle part of a Rbend is described by an Sbend. The fragmentation of Sbends is already discussed above. Thus, the fragmentation of Rbends is realized as shown in figure 3.1.
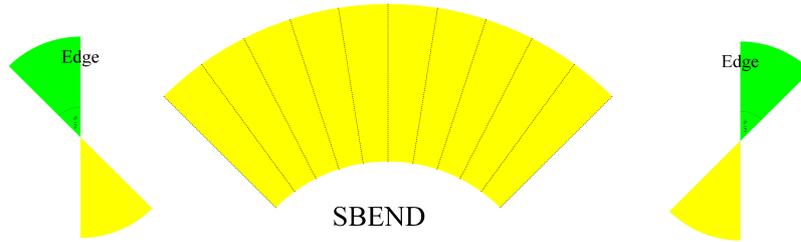
Figure 3.1:   Fragmentation of Rbends
The fragmentation of a Rbend is realized by the fragmentation of the Sbend part.

A fragmentation of Rbends by 'mini'-Rbends leads to an additional focusing effect. This effect is based on the generation of an additional field gradients.

3.2   P12 - Basics, Features and Approximations

P12 is appropriate for the calculation of lattices in high energy electron accelerators. Some elements of the transfermatrix, like R_{56}, require the momentum or the energy of the particles. The relationship of momentum, kinetic energy (E_{kin}), total energy (E) and rest energy (m_0c^2) is known from the relativistic dynamics. In P12 the average particle energy (E) is used:

$$E = \sqrt{E_{kin}^2 + m_0^2 c^4}.$$

In accelerator physics different descriptions of particle coordinates in the six-dimensional phase space are in common. In P12 the canonical coordinates are :

$$
\begin{pmatrix} x \\ x' \\ y \\ y' \\ z \\ z' \end{pmatrix} = \begin{pmatrix} x \\ \frac{p_x}{p} \\ y \\ \frac{p_y}{p} \\ \delta l \\ \frac{\Delta p}{p} \end{pmatrix}.
$$

The coordinate systems used in codes often differ in the description of the longitudinal plane. For example, MAD uses a time difference Δt instead of the longitudinal displacement δl. The definition of the coordinates determines the configuration of the σ-matrix. This matrix describes the bunch properties, which are necessary for space charge calculation. The σ-matrix elements in P12 correspond to the RMS-values of the distributions, e.g. for an upright bunch the element σ_{11} defines the second momentum of the bunch extension in x-direction, $\sqrt{\sigma_{11}} = \sigma_x$. The values of the σ-matrix arrays are given in the SI-system, e.g. $\sigma_{11}[m^2]$.
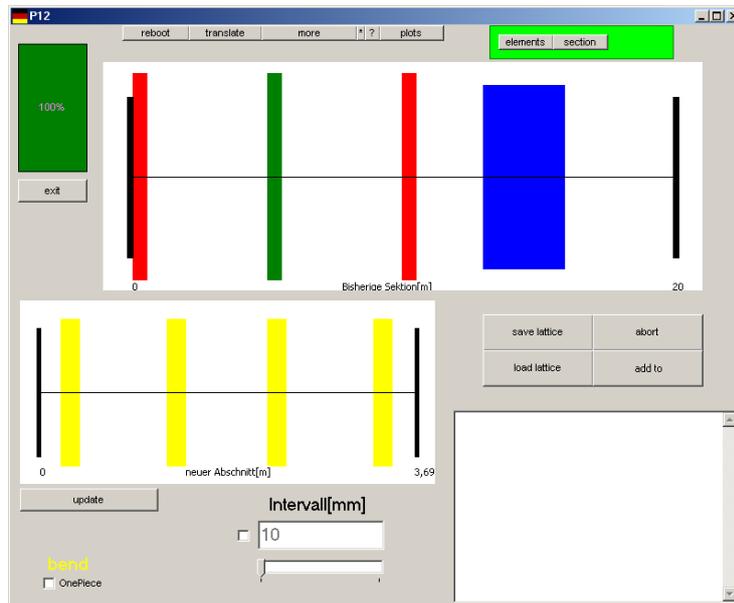
Figure 3.2:   P12 - Layout

This screen shot shows the main interface of the program P12, at which the previous lattice (above) as well as the additional lattice-part (below) are presented. The different kinds of magnetic elements are distinguished by colours.

In general, the designing of lattices is time-consuming. Therefore, special subrou-

tines in the code P12 are provided, which help to assist the progress of designing. Often precasted lattices are used, which are only adapted to the new requirements. In P12 *new* lattices can be created by *old* lattices, precasted lattices, e.g. FODO-cells, and single beam optic elements or as combinations of those three. *Old* lattices are available by the subroutine *lattice*. It is possible to test the impact of new lattice sections before adding them to the design lattice. The impact of the created lattice and the effect of new sections can be investigated by the plot subroutine.

Due to the different input decks the comparison of lattices from different pro-

(1) Plot Subroutine

(2) Translation Subroutine
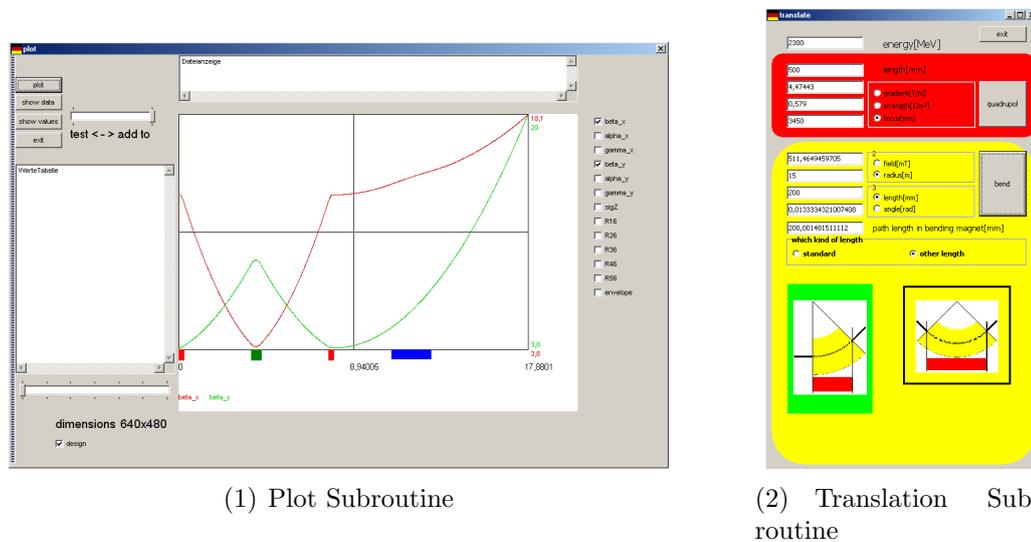
Figure 3.3: P12 - Plot Subroutine and Translation Subroutine

The plot subroutine offers the possibility to investigate the properties of the lattice and the beam development without the use of external programs. The translation subroutine is evolved from the need of the benchmarking of P12. With this subroutine different input decks can be converted into each other.

grams can become complicated. Therefore, the program P12 consists of a translation subroutine for bending magnets and for quadrupoles, fig. 3.3. Further translation algorithms are proposed. The implementation of *new* elements in P12 is provided by the subroutine *start-matrix*. The *start-matrix* is a transfermatrix, which is used at the beginning of every lattice section. If the *start-matrix* is defined to the transfermatrix of a *new* element, the impact of the *new* element is taken into account at the beginning of every section.

In the following the parameter of the different beam optic elements are presented.

Beam optics without Space Charge Effects

Drift

The element drift is characterised by only one parameter, the driftlength. This parameter defines the endpositoin of a drift as well as the possible endposition of a lattice.

Parameter	Unit	Description
lsdr	*m*	endposition

Table 3.1: Parameter of the Drifts in P12

Quadrupole

Quadrupoles are used to focus and defocus. In contrast to drifts the implementation and characterisation of quadrupoles require more input parameters. The first parameter defines the focusing plane. QF marks a quadrupole, which focuses in x-plane and QD a quadrupole, which defocuses in x-plane. A second parameter defines the starting position of the quadrupole, called $QposF$ and $QposD$. The combination of focusing strength, $QkonstF$ or $QkonstD$, and quadrupole length, lqF or lqD, determines the focal length of a quadrupole. An advantage of using the focusing strength is, that this input parameter is independent of the particle momentum. With the knowledge of the particle momentum, the focusing strength can be expressed by a field gradient [9]. Based on the dependency of focusing strength, focal length and quadrupole length the use of the focusing strength is chosen for P12.

Parameter	Unit	Description
QF/QD	-	marks the focusing plane, $QF \rightarrow$ focuses in x-direction
$QposF/QposD$	m	starting position
$QkonstF/QkonstD$	m^{-2}	focusing strength
lqF/lqD	m	length

Table 3.2: Parameters of the Quadrupoles in P12

Bends

The effect of a bends can be determined by 6 parameters. The first parameter distinguishes between Sbend(SB) and Rbend(RB). Further parameters define the position, the length and the field strength of the bending magnet. The field configuration determines the bending direction, up, down, left hand or right hand. In the lattice-file the bending directions are marked by t for true or f for false.

Example: SB 0 2 1 f f

It stands for a **Sb**end, which starts at $0m$. The field strength is 2 Tesla. The '1' marks the length of the bend of $1m$. A definition of the bend length is presented in the following. The first f defines the bending direction. The second f determines, whether the bending plane is identical to the x-z-plane or the y-z plane. This

Parameter	Unit	Description
$Bpos$	m	starting position
$Bfeld$	T	field strength
$blan$	m	length

Table 3.3: Parameters of the Bends in P12
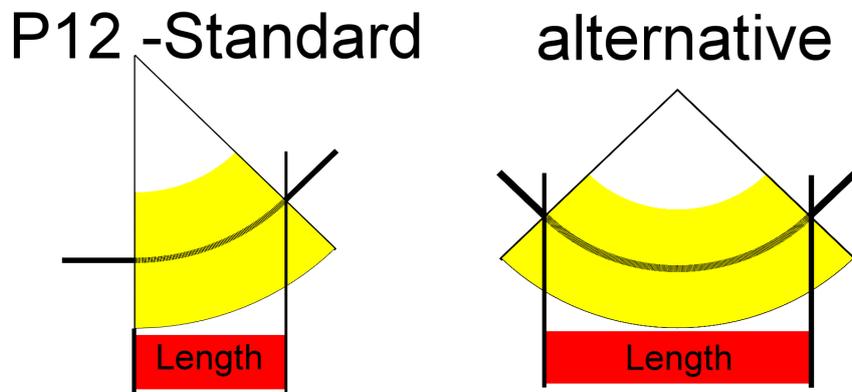
Figure 3.4: Length of Bends

Two different definitions of magnet length are in common. The scheme on the left hand side shows the definition used in P12. It bases on a projection of the design path, whereas the other definition, on the right hand side, determines the magnet length by the distance between the exit points of the design path. The relation between both lengths is given by the cosine of the bending angle.

input deck for bending magnets differs from the input decks of other programs, whose input decks contain bending radius, bending angle and path length inside the bend. Those parameters allow a calculation of the effects of bends, which is independent of any physical realisation. The motivation for the particular input deck in P12 is based on the fact, that for designing lattices the physical realisation has also been taken into account.

Undulators

Undulators are one of the main components of every FEL. They are characterised by many parameters, like pole dimensions, gapsize and in the case of elliptical APPLE undulators by the shift-parameter. With the large number of

parameters the field configuration becomes not only tunable but also complex. In chapter 2 the approximations for undulators used in P12 are discussed. In these approaches most of the real undulator parameters are not necessary. The undulators are characterised by their period length λ_u, the number of periods $Uzahl$ and their average field strength $Ufeld$. In the case of elliptical undulators the field strength is determined by two parameters, which are the average field strength in x-direction $feld1$ and the average field strength in y-direction $feld2$. In order to merge an undulator correctly into a lattice, the undulator position $Upos$ is required as well. The different kinds of undulator approximations and undulator features are selectable by three parameters, $AMundu$, $UnduGen$ and $Endpol$. These parameters are boolean, i.e. their values are *0* and *1* rather *false* and *true*. Only in the Rbend-approach and the approach for elliptical undulators
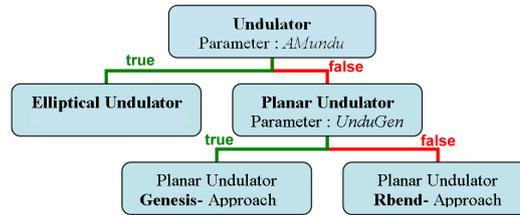
Figure 3.5:   Selection Scheme for Undulators
This scheme illustrates the construction of the undulator-selection procedure in P12.

endpoles are available. In section 2.2 different kinds of realization of endpoles are introduced. In the code P12 the endpole configuration is characterised by a constant magnetic-pole length with a variable field strength. The endpoles are computed with full undulator periods, whereby the length of the undulators remains constant, regardless of whether the endpoles are set or not.

Parameter	Unit	Description
UE/UP	$-$	marks the different kinds of undulator types, UE = elliptical undulator UP = planar undulator
$Upos$	m	starting position
$Ufeld$	$-$	RMS K-value/field strength of **planar** undulators
$feld1/feld2$	T	(average) field strengths of **elliptical** undulators in x- and y-direction
λ_u	m	period length
$Uzahl$	$-$	number of periods

Table 3.4: Parameters of the Undulators in P12

Approximations in the Space Charge Calculation

The space charge fields are determined by eq. 2.34 and eq. 2.35. These equations contain the parameters a, b and I, which describe the dimensions of the bunch and the peak current. The bunch profile is given by the σ-matrix. In P12 the data of the σ-matrix corresponds to the RMS-values of distributions. That means, the parameters a and b are given by $\sqrt{5} \cdot \sigma_x$ and $\sqrt{5} \cdot \sigma_y$, as the equivalent beam model is used. These parameters describe the transversal dimensions of the bunch. The longitudinal dimension of the bunch is used to transform the parameter I, which corresponds to the peak current:

$$I = \frac{3Q\beta c}{4\sqrt{5}\sigma_z}.$$

Q relates to the bunch charge and βc corresponds to the average bunch velocity. The development of this formula is presented in appendix B. In case of a rotated bunch the projections on the axes of the reference system are used.
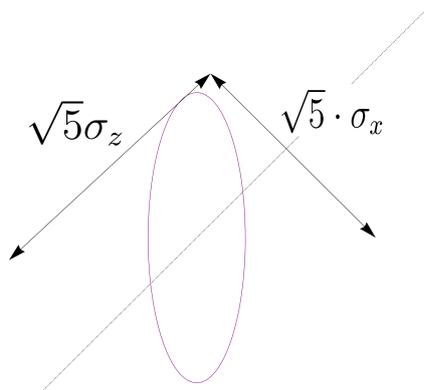
Figure 3.6:   Bunch Dimensions of a Rotated Bunch
Since the code P12 does not consist of any subroutines for the calculation of longitudinal space charge effects, the assumption of a deformation is accepted.

If the bunch is rotated according to the reference system, the resulting space charge effects of different planes will couple. Since the code P12 does not contain any subroutines for the calculation of longitudinal space charge effects, the assumption of a deformation is accepted. This leads to a slightly different calculation of space charge effects. In the sections 2.4.1 and 2.4.2 that topic has been discussed in detail.

4

Benchmarking

In this chapter the validity of the results of the code P12 is shown by the comparison with different established programs. Since the space-charge calculation in the code P12 is based on the development of bunches without the impact of space charge, the correct computations of the bunch development excluding space charge is required. The code MAD, Methodical Accelerator Design, is an established program for the computation of magnetic lattices including also second order effects. The comparison of the results of P12 with the results of MAD will demonstrate the reliability of the P12-simulation routine, while space charge effects are excluded.

The main task of the code Genesis1.3 is the simulation of the FEL-process. P12 was planned for fast design and calculation of beam optics for Genesis1.3. So the results of P12 have to correspond to those of Genesis1.3 as well. Genesis1.3 is equipped with a special element, undulator, which is treated in a particular way, as mentioned in section 2.2. In P12 different types of undulators are computable, including also the undulator model of Genesis. The validity of the undulator focusing in P12 was checked by the comparison with the code WAVE [25].

The space charge calculation is tested with Trace3D and ASTRA. Trace3D is a fast, analytically calculating program. It copes with the elements of beam optics as well as with space charge effects in a linear manner. The output data of Trace3D consists among others also of a transfermatrix. In this chapter, the transfermatrices calculated by P12 and by Trace3D are compared and discussed. For the investigation of higher order space charge impacts the code ASTRA, A Space Charge Tracking Algorithm, can be used. ASTRA is a particle tracking program, whose main task is the calculation of space charge effects and their impact on charge distributions in return. A comparison of tracking programs with analytically calculating programs is hard to manage. In general, analytical programs, like Trace3D and P12, use approximations and approaches, which simplify the elements compared to numerical calculations. This can cause discrepancies. An example for these approximations is the 'hard edge' approach for magnetic elements. Instead of using elements with fringing fields, the elements are approached by effective field lengths and effective field strengths. In this 'hard edge' approximation the deviation of the field distributions tends to infinity at the border of the elements. Such approximations can create singularities, which leads to numerical errors. Thus, the comparison between numerical simulations and analytical calculations has to be performed very carefully.

4.1 MAD

In absence of space charge fields the correct computing of the transfermatrices is checked with MAD. The results of P12 are presented with additional decimal places to show the trends rather than suggesting a higher accuracy. All magnetic elements involved in P12, except the undulators, are benchmarked with MAD. It uses a special coordinate system, which differs from the coordinate system of P12 in longitudinal direction. The values of the dispersion elements in P12 have to be divided by β to yield the values of the dispersion elements in MAD. Another source of variations are the differences in the input decks of both codes. MAD uses parameter, which are independent of the particle properties and the mechanical layouts. P12 is designed for creating lattices with 'external' parameters. In the case of quadrupoles, the input parameters are the same. Both use focusing strength and length of quadrupoles. However, the input deck for the calculation of bending magnets differs. MAD uses the bending angle and the path length inside the magnet. These parameters determinate the curvature radius. The input deck of P12 consists of the magnetic field strength and the length of the bending magnet.

Bends

<div align="center">

SBEND

</div>

The average particle energy is $2300 MeV$. Other input parameters are a magnetic field strength of $803,41$mT and a length of the bending magnet of $8,270$m. This yields to a curvature radius of $9,55$m and a bending angle of $\frac{\pi}{3}$.

<div align="center">

MAD

</div>

$$\begin{pmatrix} 0.500000 & 8.269933 & 0 & 0 & 0 & 4.774648 \\ -0.090690 & 0.500000 & 0 & 0 & 0 & 0.866025 \\ 0 & 0 & 1 & 10 & 0 & 0 \\ 0 & 0 & 0 & 1 & 0 & 0 \\ -0.866025 & -4.774648 & 0 & 0 & 1 & -1.730066 \\ 0 & 0 & 0 & 0 & 0 & 1 \end{pmatrix}$$

<div align="center">

P12

</div>

$$\begin{pmatrix} 0.500000 & 8.26993343 & 0 & 0 & 0 & 4.77464828 \\ -0.09068997 & 0.500000 & 0 & 0 & 0 & 0.8660254 \\ 0 & 0 & 1 & 9.999999994 & 0 & 0 \\ 0 & 0 & 0 & 1 & 0 & 0 \\ -0.8660254 & -4.77464828 & 0 & 0 & 1 & -1.73006706 \\ 0 & 0 & 0 & 0 & 0 & 1 \end{pmatrix}$$

RBEND

In contrast to the Sbend, the particle beam does not enter or leave the Rbend perpendicular. In this example the Rbend is characterised by two symmetrical angles of entrance and exit, which correspond to the half of the bending angle. The average particle energy is defined to $2300MeV$. The other input parameters are a magnetic field strength of 2008,54mT and a length of the bending magnet of 2,7m. This yields to a curvature radius of 3,82m and a bending angle of $\frac{\pi}{4}$.

MAD

$$\begin{pmatrix} 1 & 2.700949 & 0 & 0 & 0 & 1.118770 \\ 0 & 1 & 0 & 0 & 0 & 0.828427 \\ 0 & 0 & 0.674677 & 3 & 0 & 0 \\ 0 & 0 & -0.181603 & 0.674677 & 0 & 0 \\ -0.828427 & -1.118770 & 0 & 0 & 1 & -0.299051 \\ 0 & 0 & 0 & 0 & 0 & 1 \end{pmatrix}$$

P12

$$\begin{pmatrix} 1 & 2.70094895 & 0 & 0 & 0 & 1.11876969 \\ 0 & 1 & 0 & 0 & 0 & 0.82842712 \\ 0 & 0 & 0.67467743 & 3 & 0 & 0 \\ 0 & 0 & -0.18160346 & 0.67467743 & 0 & 0 \\ -0.82842712 & -1.11876969 & 0 & 0 & 1 & -0.2990512 \\ 0 & 0 & 0 & 0 & 0 & 1 \end{pmatrix}$$

The impact of fringing fields is implemented as discussed in [10]. In a linear manner the impact of edge focusing also depends on external parameter, i.e. gapsize. In contrast to this example the values of edge focusing and defocusing (different planes) can differ from each other. It is based on the effects of the gapsize between the magnetic poles, which modifies the resulting fringing fields.

Quadrupoles

A quadrupole with a focusing strength of $0.5797\frac{1}{m^2}$ and a length of $250mm$ is chosen to benchmark the results of MAD and P12. It focuses in x-plane. The average particle energy is $200MeV$.

<div align="center">MAD</div>

$$
\begin{pmatrix}
0.981939 & 0.248493 & 0 & 0 & 0 & 0 \\
-0.144051 & 0.981939 & 0 & 0 & 0 & 0 \\
0 & 0 & 1.018170 & 0.251512 & 0 & 0 \\
0 & 0 & 0.145802 & 1.018170 & 0 & 0 \\
0 & 0 & 0 & 0 & 1 & 2E-6 \\
0 & 0 & 0 & 0 & 0 & 1
\end{pmatrix}
$$

<div align="center">P12</div>

$$
\begin{pmatrix}
0.98193900 & 0.248493097 & 0 & 0 & 0 & 0 \\
-0.14405145 & 0.98193900 & 0 & 0 & 0 & 0 \\
0 & 0 & 1.01817039 & 0.25151223 & 0 & 0 \\
0 & 0 & 0.145801722 & 1.01817039 & 0 & 0 \\
0 & 0 & 0 & 0 & 1 & 1.632E-6 \\
0 & 0 & 0 & 0 & 0 & 1
\end{pmatrix}
$$

The difference in the element R_{56} results from different definitions of the coordinate system. Furthermore, in this example the value of the element R_{56} is rounded up. In the case of a bending magnets the conversion is more complex, because the element R_{56} contains more components than the relativistic deviation, see app. A.

MAD also calculates the development of input data, like TWISS-parameters. Figure 4.1 shows the development of the *beta*-function along a chicane. This chicane consists of 4 bending magnets with different entrance angles, figure 4.2. All magnets have the same characteristics, i.e. the same magnetic field strength and the same magnetic length. A beam enters the first magnet perpendicular and leaves it by the angle of bending. The second magnet is entered by the angle of exit of the first magnet and leaves perpendicular. This chicane is symmetrical and so the third bend is entered perpendicular again and so on. The results of P12 correspond to the results of MAD. Furthermore, figure 4.1 also shows that in general the development of the bunch dimensions cannot be calculated by a linear approximation between two separated points. Thus, the computation of space charge effects requires a calculation of intermediate points.
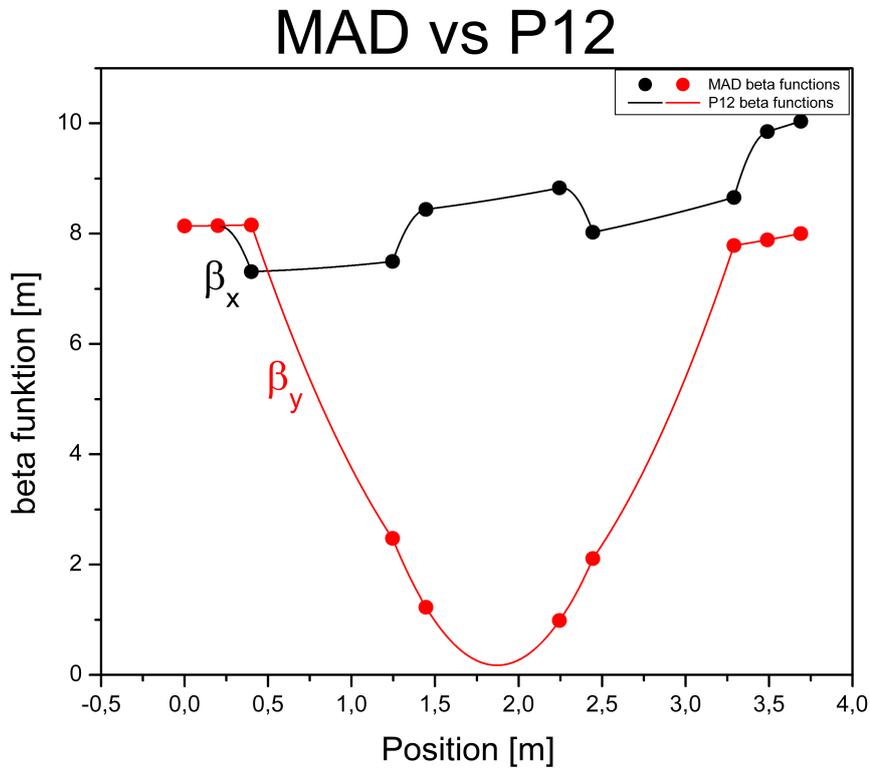
Figure 4.1:   Beta-Function Development

This plot shows the development of the β-function in x-plane and y-plane along a chicane used for bunch compression. The function of P12 corresponds to the points of MAD.

Figure 4.2:   Chicane Design Scheme

Such magnetic arrangements are used to compress bunches. The principle of this scheme bases on a combination of the dispersive effect and the energy chirp along the bunch.

4.2   Genesis1.3

In contrast to MAD, Genesis1.3 is a particle tracking program. The main task of Genesis1.3 is the simulation of the FEL-process. Due to the fact that the bunch dimensions have a strong impact on the FEL-process, the development of the

bunch dimensions are also a part of the Genesis calculation routine.

Figure 4.3 shows the development of the beam cross section along a good matched FODO-lattice. This lattice is composed of four regular FODO-cells, i.e. it consists of nine alternating quadrupoles with an equal distance between two quadrupoles. Each distance between two quadrupoles amounts to $3.45m$. The quadrupole length is $0.5m$. A focal length of $3.45m$ leads to a focusing strength of $0.58\frac{1}{m^2}$. The particle energy is set to the maximum value of the planned BESSY FEL, 2.3GeV. Other beam parameters are the RMS-cross section $50\mu m$ and the transversal normalised emittance of $1.5mm\ mrad$. The results of Genesis1.3 and P12 are
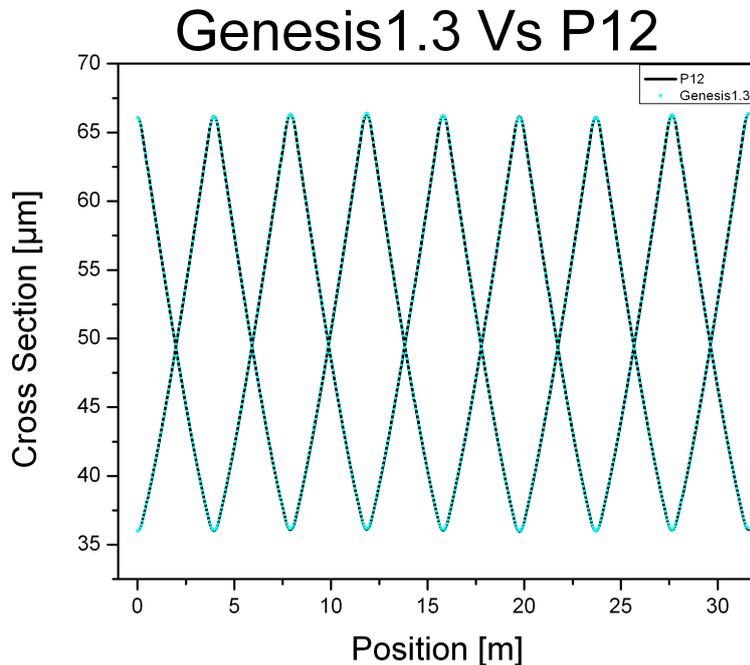
Figure 4.3:   FODO-Lattice with Good Matching

This plot shows a good matched FODO-lattice. The amplitude of the betatron oscillation has to be controlled for a good matching.

identical. There is a perfect matching between the FODO-lattice and the initial beam parameters. In contrast to figure 4.3, figure 4.4 shows a dismatching between the FODO-lattice and the initial beam parameters.

 If there is a dismatch, the dimensions of the beam cross section will increase, as shown in figure 4.4. The calculations of this lattice by P12 are also affirmed by Genesis. For the simulation of the FEL-process, Genesis1.3 has to include undulators. Different treatments of undulators are already presented in chapter 2.2. In figure 4.5, the different approaches of planar undulators are compared with each other. The output data from Genesis1.3, from P12 with the Genesis1.3
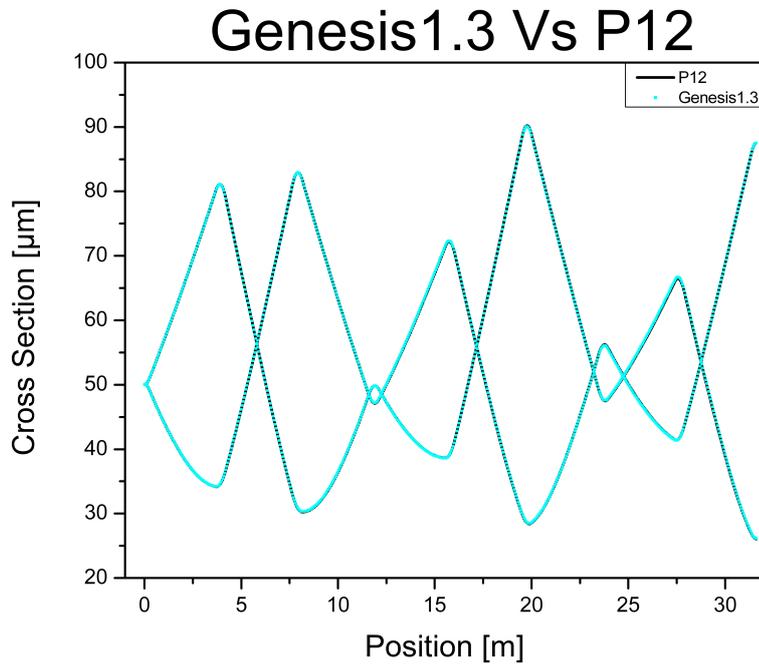
Figure 4.4: Dismatched FODO-Lattice

This plot shows a dismatch between lattice and initial beam parameter. The RMS beam size increases along several FODO cells.

undulator approach and from P12 with the Rbend approach are shown. The undulator consists of 69 period with a period length λ_u of 50 mm. The undulator RMS K-value is 3.

The results show a very good agreement. As discussed in chapter 2, planar undulators act like combinations of focusing planes of quadrupoles and drifts. In planar undulator the focusing plane is not the plane of bending.
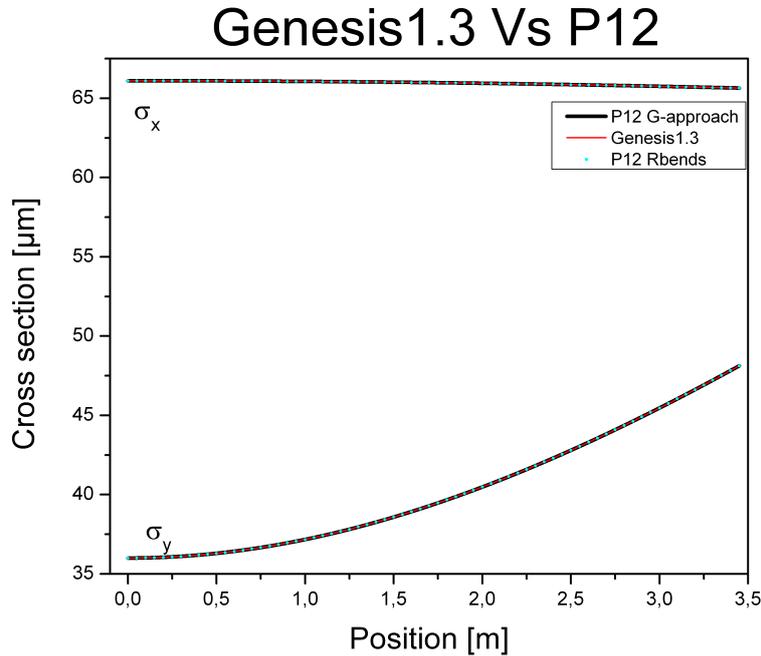
Figure 4.5: Comparison of different Undulator Approaches

In this plot the correspondence of the transverse focusing characteristics of the different undulator approaches is shown.

4.3 Trace3D

The space charge force changes the development of the bunch. In a linear approximation the space charge force can be seen as an additional defocusing force. There are different approaches for the implementation of space charge effects. Trace3D calculates in a linear manner and uses 'space charge kicks' [22]. Each element in the lattice splits up. Between the pieces of elements, the defocusing effect is added by a change of divergence, i.e. kick. Due to this approximation the treatment of all elements remains identical to calculation without space charge effect. The third version of 'trace' (Trace3D) consists of a 3D space-charge calculating subroutine. An application area for Trace3D is the calculation of beam dynamics in Energy Recovery Linacs (ERL), including low energy sections and chicanes. Chicanes are often used to compress bunches in longitudinal direction. If a bunch has to be compressed to its limit, the repulsing force of space charge effects appears as a limiting factor. In the last part of this section the results of space charge testes in a chicane are presented.

DRIFT

For a first comparison a lattice with a drift of 1m is chosen, because the impact of the space charge effects cannot be manipulated by any external fields. The regular transfermatrices of both programs agree totally. Beam parameters are a circular cross section with a radius (RMS) of $0.8mm$, a RMS bunch length of about $3mm$, a bunch charge of $77pC$ and an average particle energy of $6.5MeV$.

DRIFT - Without Space Charge Effects

$$\begin{pmatrix} 1 & 1 & 0 & 0 & 0 & 0 \\ 0 & 1 & 0 & 0 & 0 & 0 \\ 0 & 0 & 1 & 1 & 0 & 0 \\ 0 & 0 & 0 & 1 & 0 & 0 \\ 0 & 0 & 0 & 0 & 1 & 0.0061804 \\ 0 & 0 & 0 & 0 & 0 & 1 \end{pmatrix}$$

DRIFT - With Space Charge Effects
P12

$$\begin{pmatrix} 1.02306 & 1.007615 & 0 & 0 & 0 & 0 \\ 0.04584 & 1.02261 & 0 & 0 & 0 & 0 \\ 0 & 0 & 1.02306 & 1.007615 & 0 & 0 \\ 0 & 0 & 0.04584 & 1.02261 & 0 & 0 \\ 0 & 0 & 0 & 0 & 1 & 0.0061804 \\ 0 & 0 & 0 & 0 & 0 & 1 \end{pmatrix}$$

TRACE3D

$$\begin{pmatrix} 1.02305 & 1.007611 & 0 & 0 & 0 & 0 \\ 0.04582 & 1.02259 & 0 & 0 & 0 & 0 \\ 0 & 0 & 1.02305 & 1.007611 & 0 & 0 \\ 0 & 0 & 0.04582 & 1.02259 & 0 & 0 \\ 0 & 0 & 0 & 0 & 1.00073 & 0.0061805 \\ 0 & 0 & 0 & 0 & 0.0236 & 1.00073 \end{pmatrix}$$

Note that, in P12 the longitudinal space charge effects are not taken into account, accordingly the elements R_{55}, R_{56}, R_{65} and R_{66} do not have to agree. The comparison of the results of P12 and Trace3D shows that the transverse defocusing of P12 is slightly stronger pronounced than the defocusing of Trace3D. This is explained immediately, if the longitudinal part of the transfermatrices is considered. The chosen parameters leads to a non-vanishing longitudinal space charge effect. Due to the additional defocusing in the longitudinal direction the bunch length increases faster in Trace3D than in P12. Therefore, the average current decreases more and so does the magnitude of the transversal space charge effects. In this test the relative change between including and excluding longitudinal space charge effects is about $\frac{1}{2000}$. The dimension of the transverse cross section at the end of this lattice is $0.8244mm$, whereby the difference amounts to $400nm$.

QUADRUPOLES

At the beginning of the comparison of space charge computation in quadrupoles a single quadrupole is chosen. For the space charge calculations the following beam parameters are used. The average particle energy is $23\,MeV$, the dimensions of the bunch cross section are $0,661 \times 0,36\,mm^2$ and the bunch length is $3mm$. The quadrupole is characterised by a length of $0.5m$ and a field gradient of $0.044744\frac{T}{m}$. Results of calculations without the impact of space charge are almost identical.

Quadrupole - Without Space Charge Effects

P12

$$
\begin{pmatrix}
0.9279622 & 0.4879350 & 0 & 0 & 0 & 0 \\
-.2846406 & 0.9279622 & 0 & 0 & 0 & 0 \\
0 & 0 & 1.073810 & 0.5122422 & 0 & 0 \\
0 & 0 & 0.2988204 & 1.073810 & 0 & 0 \\
0 & 0 & 0 & 0 & 1 & 0.2468052E-3 \\
0 & 0 & 0 & 0 & 0 & 1
\end{pmatrix}
$$

TRACE3D

$$
\begin{pmatrix}
0.9279622 & 0.4879350 & 0 & 0 & 0 & 0 \\
-.2846406 & 0.9279622 & 0 & 0 & 0 & 0 \\
0 & 0 & 1.073810 & 0.5122422 & 0 & 0 \\
0 & 0 & 0.2988204 & 1.073810 & 0 & 0 \\
0 & 0 & 0 & 0 & 1 & 0.2468062E-3 \\
0 & 0 & 0 & 0 & 0 & 1
\end{pmatrix}
$$

A bunch charge of $1nC$ leads to a change in the dimensions of the cross section of round 0.5 %. This additional expansion occurs while the beam moves $0.5m$. The transfermatrix including space charge are:

Quadrupole - With Space Charge Effects

P12

$$
\begin{pmatrix}
0.93112895 & 0.48847396 & 0 & 0 & 0 & 0 \\
-0.2721009 & 0.93121987 & 0 & 0 & 0 & 0 \\
0 & 0 & 1.07976055 & 0.5132148 & 0 & 0 \\
0 & 0 & 0.32293301 & 1.0796227 & 0 & 0 \\
0 & 0 & 0 & 0 & 1 & 0.24680518E-3 \\
0 & 0 & 0 & 0 & 0 & 1
\end{pmatrix},
$$

TRACE3D

$$
\begin{pmatrix}
0.9311307 & 0.4884743 & 0 & 0 & 0 & 0 \\
-.2720939 & 0.9312217 & 0 & 0 & 0 & 0 \\
0 & 0 & 1.079764 & 0.5132154 & 0 & 0 \\
0 & 0 & 0.3229465 & 1.079626 & 0 & 0 \\
0 & 0 & 0 & 0 & 1.000001 & 0.2468063E-3 \\
0 & 0 & 0 & 0 & 0.5102915E-02 & 1.000001
\end{pmatrix}.
$$

Due to the short path length, the longitudinal dimension remains almost constant. Hence it follows, the influence of the transversal space charge values by the longitudinal space charge effects is small. The relative discrepancies in the size of the bunch cross section of the results of P12 and Trace3D are less than $\frac{1}{100}$ %.

FODO-Lattice

In order to investigate the impact of space charge effects along combinations of quadrupoles and drifts, a FODO-lattice is chosen. This kind of lattice is already presented in chapter 4.2. The particle energy is set to $23MeV$. Due to the lower particle energy the dominance of space charge increases. The focusing strength of the quadrupoles remains almost constant, but due to the change of energy the quadrupole field gradients have to be adjusted.

$$
QG(2300MeV) = 4.47443\frac{T}{m} \ \Rightarrow \ QG(23MeV) = 0.0447443\frac{T}{m}
$$

As a result of the combination of the low average particle energy and the long lattice, a change of the bunch length by the longitudinal space charge effects becomes observable, whereby the change of the longitudinal dimensions corresponds to 0.25 % of the bunch length.

FODO-lattice - including Space Charge Effects

P12

$$
\begin{pmatrix}
-1.068249 & 11.37143 & 0 & 0 & 0 & 0 \\
-0.08178167 & -0.065552 & 0 & 0 & 0 & 0 \\
0 & 0 & -1.1542979 & 2.8276633 & 0 & 0 \\
0 & 0 & -0.2954681 & -0.1425245 & 0 & 0 \\
0 & 0 & 0 & 0 & 1 & 0.015598088 \\
0 & 0 & 0 & 0 & 0 & 1
\end{pmatrix}
$$

TRACE3D

$$
\begin{pmatrix}
-1.068410 & 11.36073 & 0 & 0 & 0 & 0 \\
-0.08179253 & -0.06624522 & 0 & 0 & 0 & 0 \\
0 & 0 & -1.154480 & 2.823486 & 0 & 0 \\
0 & 0 & -.2955562 & -.1433557 & 0 & 0 \\
0 & 0 & 0 & 0 & 1.002317 & 0.01561005 \\
0 & 0 & 0 & 0 & 0.2992545 & 1.002349
\end{pmatrix}
$$

The dimensions of the cross section are defined by the values of the semi axes (RMS-values)

$$\sigma_x(0m) \approx 0.67\,mm \qquad \text{and} \qquad \sigma_y(0m) \approx 0.36\,mm \quad initial,$$
$$\sigma_x(10m) \approx 0.91\,mm \qquad \text{and} \qquad \sigma_y(10m) \approx 0.49\,mm \quad final.$$

The differences between the initial values and the final values are small. It seems that the space charge effects have only a weak effect on the beam and change its properties only a little. But the development of the beam size shows another effect. Unfortunately, there was no output of Trace3D, which suffice for a plot with both programs. The figure 4.6 bases on data from P12.
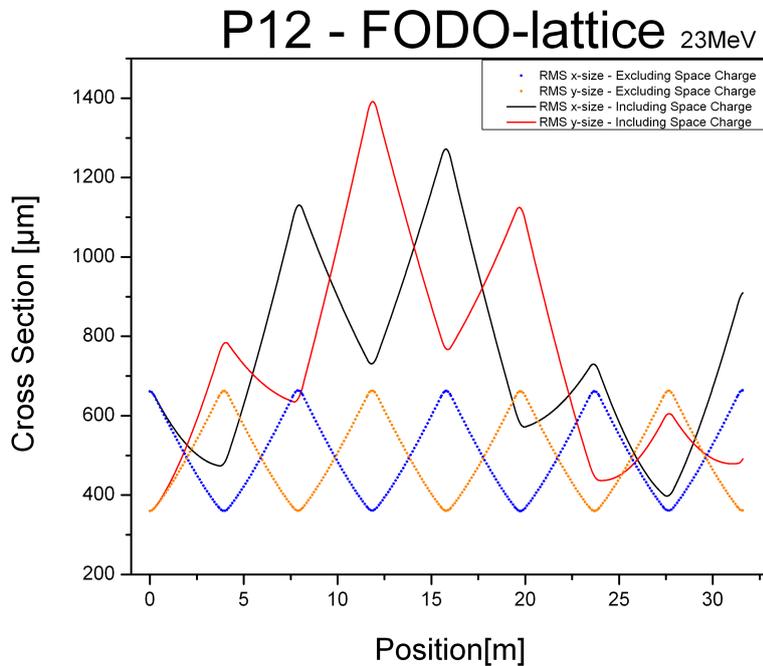
Figure 4.6: RMS-Beam Size Development and Space Charge Effects
This plot shows the different developments of the beam cross section with and without the impact of transverse space charge effects. The impact of space charge leads to a dismatch between the characteristics of the lattice and the dynamics of the bunch.

This plot presents the development of the transverse RMS beam size including and excluding transverse space charge effects. In this plot an important feature of beam focusing is shown. The focusing effect becomes stronger, if the dimensions of the beam cross section increase. Due to the space charge defocusing a dismatch between the characteristics of the lattices and the dynamics of the

bunch is created. This leads to a beat of the beta-function and so to a beat of the bunch dimensions. As a consequence, the beam focuses at several spots, at which the beam cross section becomes smaller than in the case of a good matching. In figure 4.6 one spot is located at about $28m$. But in return, after passing this spot the bunch cross section increases rapidly. Thus, the transfermatrices with space charge defocusing could even show a smaller bunch cross section than transfermatrices without space charge defocusing do.

Bends and Chicanes

Space charge effects in bends are complex. In the limit of a infinitesimal step size the approach of space charge 'kicks' would in theory supply correct results. Due to the physical properties of bends the dynamics of separate planes become complex. As a consequence of the characteristics of bending magnets, the longitudinal space charge effects will have an influence on the transversal dynamics of the beam and vice versa. Since the program P12 is created for the estimation of transversal space charge effects in high-energy multi-stage FELs, like STARS and FLASH II, the longitudinal space charge effects are neglected. This restriction results to a misestimation of space charge effects in the low energy regime. The dominance of the longitudinal space charge effects depends linearly on the space charge factor. Thus, at higher energy regimes the dominance of the longitudinal space charge impacts decreases. The following test is characterised by a vanishing longitudinal space charge impact. It is achieved by a long bunch at a high energy regime. The lattice design corresponds to the chicane scheme, introduced in section 4.1. For this test the bunch does not contain an energy chirp, whereby the compressing effect of the chicane vanishes. A similar lattice is intended for the bunch compression in STARS. The average particle energy is $325 MeV$. The bunch cross section is circular with the radius (RMS) of $0.1mm$ and the longitudinal dimension (RMS) of the bunch is $0.5mm$. The calculations of P12 and Trace3D yield almost identical final dimensions of the bunch and similar transfermatrix elements. But the correlation element σ_{15} differs. It is probably based on the neglecting of the longitudinal space charge impact. Nevertheless, another feature of space charge effects is demonstrated by both programs.
The impact of space charge can lead to the generation of additional dispersive terms, like shown in figure 4.7. The dispersion value increases in dependency of the bunch charge. From this follows that the chicanes have to be adjusted to the expected space charge fields as well.

Change of R16/Dispersion
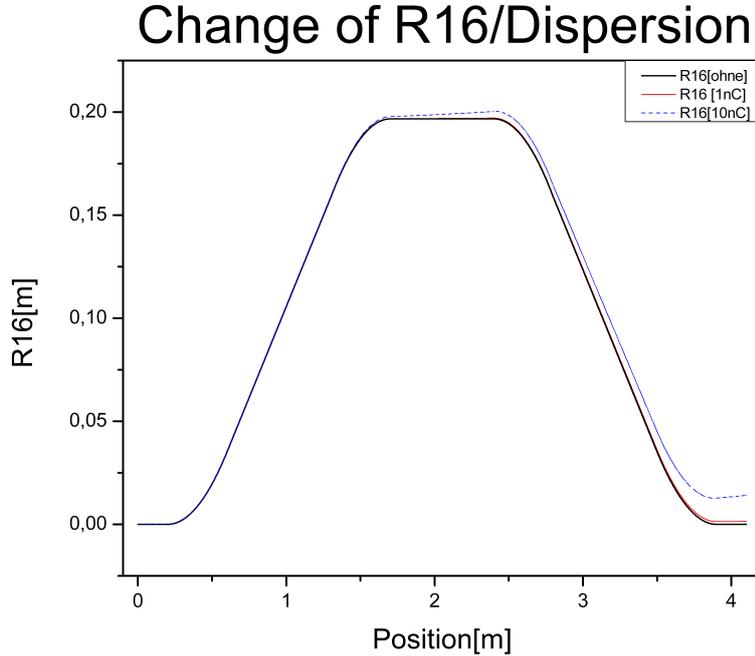
Figure 4.7: Impact of Space Charge Effects on Dispersion

This plot shows the development of the dispersive element R_{16} along a chicane for three different bunch charges. In the case of excluding space charge effects the dispersion at the end of the chicane is balanced. In the case of including space charge at the end of the lattice the dispersion is unbalanced.

4.4 ASTRA

ASTRA is a particle tracking program, whose main task is to calculate space charge effects and their impacts on the charge distributions in return. The mean range of applications is the simulation of the development of bunches in first accelerator stages, like rf-guns and further accelerator cavities. ASTRA calculates with 'macro'-particles to accomplish the high number of elementary particles. The first test of consistence of the simulation of the impacts of space charge effects is performed at a drift lattice. Further tests should prove a correct computing of space charge effects in quadrupoles. Unfortunately, a comparison of the results of particle tracking programs with the results of analytical programs is hard to manage. The correct comparison of the results requires identical input data for both programs. Analytical programs, like P12, use approaches and approximations to simplify the calculation. The hard edge approximation merges the effects of fringing fields and the 'main'-fields to effective values. Due to this approach, the field distribution becomes discontinuous. The derivation of the field distributions

tends to infinity at the border of the element. In particle tracking programs, like ASTRA, such singularities often produce numerical errors. Moreover, the development of second moments of different distributions are similar, but not identical [21]. The code P12 bases on the equivalent beam model while the results of the simulations of ASTRA are generated with a gaussian charge distribution. As a consequence the results of the simulations can differ from each other. Nevertheless, the results of both programs should show a similar development of the RMS beam size. For consistency a long FODO-lattice is tested. All tests are performed in a lower energy regime. The average particle energy is around some tens of MeV. This leads to a higher dominance of space charge effects.

DRIFT 10m

A drift element is suitable in order to demonstrate the effect of space charge, as the defocusing effect of space charge will not influenced by any external focusing parameters. Figure 4.8 shows the development of a beam cross section with and without the impact of space charge defocusing in a drift. The parameters are a average particle energy of $6.5 MeV$, a radius of the beam cross section at the beginning of the drift of $0.8 mm$, bunch length of $3 mm$, the bunch charge of $77 nC$ and transversal, γ normalised emittance of to $1 mm\, mrad$.
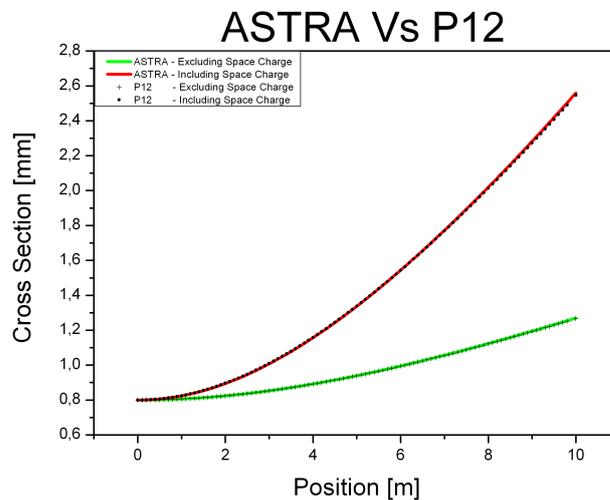
Figure 4.8: Development of the Bunch Cross Section along a Drift Lattice
In this figure the different development of the dimensions of the bunch cross section including and excluding space charge effects is shown. The dimensions of the cross section with space charge increase up to 200 % of the dimensions of the beam cross section without the impact of space charge.

In figure 4.8, a good agreement between the results of ASTRA and P12 for the drift section is presented. In the case of a low value of the ratio of energy spread and average particle energy, the bunch length remains constant while longitudinal space charge effects are excluded. Including longitudinal space charge effects the bunch length changes, figure 4.9. As a consequence the space charge factor can change.
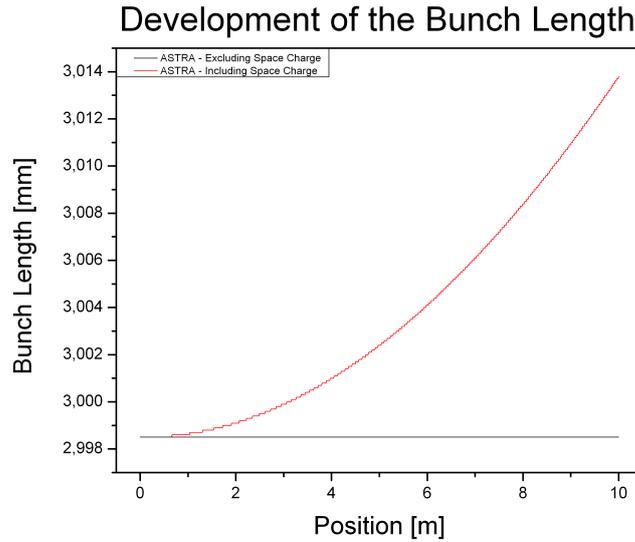
Figure 4.9:   Bunch Length Changes along a 10m Drift
This plot shows the changing of bunch length caused by longitudinal space charge effects.

Quadrupole

In order to test the correct calculation of space charge effects in quadrupoles, a special lattice is created. This lattice consists of a quadrupole surrounded by two $0.25m$ drifts . The quadrupole focuses in x-direction with a focusing strength of $0.52m^{-2}$, which yields a focus of $3.836m$ (quadrupole length $= 0.5m$). For a strong impact of space charge effects the average particle energy is set to $23MeV$. A change of the longitudinal bunch dimension is dominated by the longitudinal space charge effect. Tracking programs often struggle with numerical errors produced by singularities, like hard edge approach. Outside the quadrupole, the further development of the beam cross section can be used for an estimation of the transition impact.
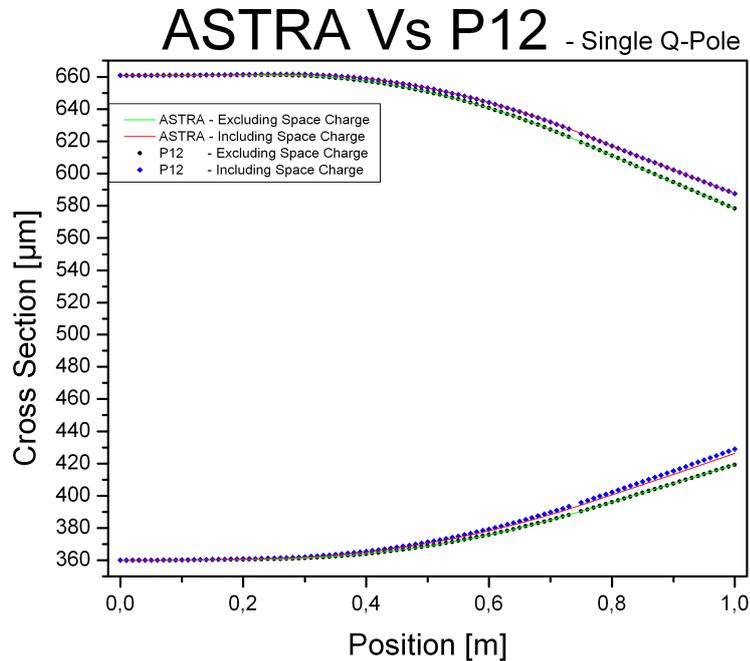
Figure 4.10:   Bunch Cross Section Development in Drift-Quadrupole-Drift-Lattice
In this plot the developments of the dimensions of the bunch cross section including and excluding space charge are shown.

The results of the calculation of a quadrupole by ASTRA and P12 without space charge impacts agree. The results of the space charge test show some slight differences, see figure 4.10. For the RMS beam size in x-direction, there is a perfect matching between P12 and ASTRA. A dismatch is shown in y-direction inside the quadrupole. This could be related to the transition from the drift to the quadrupole field.

FODO-Lattice

In order to test the correct calculation of space charge effects in combinations of many quadrupoles and drifts, the FODO-lattice, which was already introduced in chapter 4.3 , is used. Furthermore, the parameters of the beam as well as the parameter of the lattices remain the same, see chapter 4.3. While the space charge effects are neglected, ASTRA and P12 demonstrate a perfect matching, figure 4.11. A similar, but not identical, development of the bunch cross section is shown in figure 4.11, while space charge effects are included. The space charge effects generate a dismatch between lattice design and beam, which leads to a beat. Small deviations in lattice design, bunch properties or the calculation
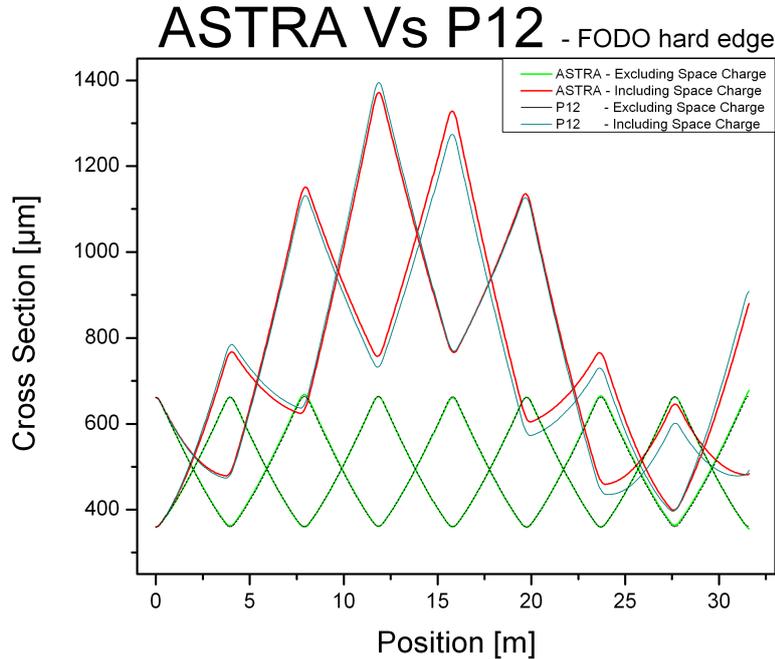
Figure 4.11:   Bunch Cross Section Development along a 4×FODO-Lattice
At the low energy regime the defocusing effects of space charge change significantly the development of the bunch cross section.

of space charge effects can cause a greater deviation in the development of the bunch. This FODO-lattice test is also performed in higher energy regimes. At a high energy regime, e.g. 1GeV, the impact of space charge can decrease to a level, where the beam remains matched to the lattice. Since the differences between the beam cross sections including and excluding space charge effects is small, the deviations are compared. In figure 4.12 the development of the beam size deviation produced by space charge effects is plotted. The results of ASTRA corresponds to the results of P12. But this test is not that meaningful. ASTRA is a particle tracking program and P12 calculates analytical, i.e. the lattices of both program differs. The simulation of the complex field-constructions, which are included in ASTRA, is not possible with P12, whereas the hard edge approximation of analytical programs generates numerical errors in the code of ASTRA. Since the numerical errors are small, they can be neglected under certain circumstances. The hard edge approximation is not applicable for this test, because the results of the test are in the same order of magnitude of the produced errors or even smaller. Due to the modified field distribution the development of the bunch size changes slightly. The maximum of the relative discrepancy of the beam size amounts to 2 %, which might have affected the result. Nevertheless, the figure 4.11 demon-
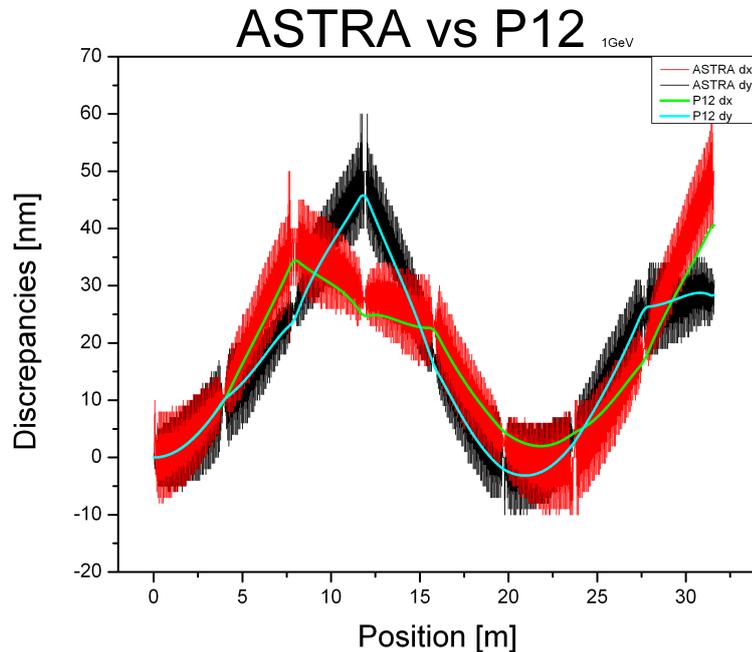
Figure 4.12:   Development of the Beam Size Deviation along a 4×FODO-Lattice
This plot shows the development of the beam size deviations produced by space charge effects.

strates the need of including space charge effects in simulations for reliable results.

4.5   WAVE

'WAVE' is a program created at BESSY [25], which calculates focusing effects as well as coupling effects in the transverse plane of undulators. The results are determined by fast tracking. This program consists of many different modes for the treatment of undulators. For the test of the undulator models of P12 analytical models are used in WAVE. The approximations of the undulators in P12 are similar to the 'Halbach'-models in WAVE. Tests with planar undulators have shown good agreements. In the case of elliptical undulators, the tests become difficult for arbitrary polarisations. The field distribution as well as the peak-values of the magnetic field strength are very sensitive to parameters like shifting and gap. For the benchmarking some examples, where the assumptions made in the code P12 are valid, are created. The boundary conditions of a test are an average particle energy of 2300MeV, no endpoles, a field strength in x of $\sqrt{2}T$,

a field strength in y of $0.5\sqrt{2}T$ and 59 periods. The transfermatrices of P12 and WAVE show a good agreement. The transfermatrices are:

$$\text{WAVE}$$

$$
\begin{pmatrix}
0.9632577 & 2.913791 & 2.995E-7 & -4.519E-6 \\
-2.47512E-2 & 0.9632649 & 5.081E-6 & 7.375E-6 \\
9.756E-6 & 2.14E-5 & 0.8557636 & 2.806757 \\
4.894E-6 & 7.355E-6 & -9.5367439E-2 & 0.855711
\end{pmatrix},
$$

$$\text{P12}$$

$$
\begin{pmatrix}
0.963263659 & 2.913793 & 0 & 0 & 0 & -5.2905E-7 \\
-2.47523E-2 & 0.963263659 & 0 & 0 & 0 & -3.564639E-7 \\
0 & 0 & 0.8557542 & 2.8067421 & 0 & -1.03866E-6 \\
0 & 0 & -0.095372 & 0.8557542 & 0 & -6.86739E-7 \\
3.564639E-7 & 5.2905E-7 & 6.86739E-7 & 1.03866E-6 & 1 & 7.2439E-6 \\
0 & 0 & 0 & 0 & 0 & 1
\end{pmatrix}.
$$

Further tests and discussions with undulator experts at BESSY confirm that in these approximations the focusing of undulators with and without shifted rows of magnets are the same, as long as the RMS-fields strength remain identical. Thus, the undulator subroutine for elliptical undulators in P12 can be used for the determination of the focusing effect of elliptical electron path designed undulators as well as of undulators with a planar, but rotated plane of motion for charged particles.
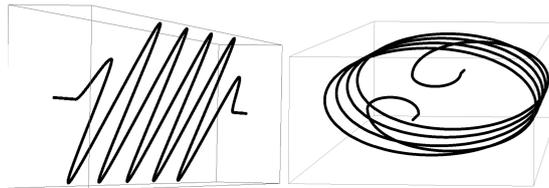
Figure 4.13: Rotated Plane Motion and Elliptical Motion
This figure displays the different kinds of paths through undulators (with endpoles).

Note that, in P12 the field strength as well as the undulator K-value are RMS-values. The field distribution is assumed by a sinusoidal function (in P12). That means, the peak value of magnetic strength, used in WAVE, corresponds to $\sqrt{2}\cdot$ RMS-value of magnetic strength in P12. The same is valid for the undulator parameter.

5

HGHG-Structures

The title of this work is *Space Charge Effects in cascaded HGHG-FELs.* So far only the space charge effects in accelerator optics are discussed. In the following a short description of the FEL-physics introduces the conjunction of beam optics and FEL-performance. Furthermore, the impact of transversal space-charge effects is investigated at two future FEL-projects, STARS and FLASH II. The performances of these FELs are tested with the simulation code Genesis1.3. Therefore, the transverse space charge defocusing was implemented in Genesis1.3. The code Genesis1.3 provides two different calculation schemes, i.e time-dependent and time-independent calculation mode. The time-dependent calculation algorithm is required for the simulation of effects like superradiance, which is expected in the radiators of the second stages of FLASH II and STARS. Since there is no superradiance expected in the first stages of FLASH II and STARS, the simulation of the FEL-process can be performed with the time-independent algorithm. To demonstrate the differences between both algorithms, the time-dependent calculation algorithm is used for the simulation of FLASH II and the simulation of STARS is performed with the time-independent algorithm.

The combination of undulator configuration and properties of the used electron bunch determines the resonance frequency of the undulator [8]:

$$\lambda_{res} = \frac{\lambda_u}{2\gamma^2}(1 + K^2). \tag{5.1}$$

The resonance frequency λ_{res} is defined by the undulator period λ_u, the undulator parameter K and the average particle energy, expressed by γ. The radiation output properties of the High-Gain FELs are characterised by two competing processes, coherent radiation and shot noise [26],[27]. Nevertheless, all radiation within a frequency range near the resonance frequency becomes amplified. Here, the density fluctuations inside the bunch define the final frequency spectrum. In the case of SASE-FELS, Self-Amplified Spontaneous Emission, this leads to a wide spectrum. For a better frequency spectrum several seeding schemes, e.g. HGHG-FEL scheme, have been developed. The process of seeding establishes an energy modulation along the bunch. Due to the impact of dispersion this energy modulation leads to a density modulation, called microbunching. The structure of microbunches depends of the wavelength of the seeding radiation λ_{seed} [28]. Unfortunately, high-power, short-wavelength LASER sources for seeding are not available. This lack can be bypassed by shifting the frequency up-conversion in the FEL-process as proposed for the HGHG-FEL scheme. In the HGHG-FEL scheme

several undulator types with different resonance frequencies are combined to one FEL. In the case of FLASH II, there are two HGHG-stages, each consisting of two different undulator types, merged to one FEL-facility.

In the first stage the rear part of the electron bunch is used for generating the seed radiation for the second stage. The seeded part of the bunch becomes energy modulated in the first undulator, called modulator, i.e. it becomes seeded. Due the the impact of dispersion this energy modulation leads to a density modulation, called microbunching. The microbunching can be optimised for a certain harmonic of the seeding wavelength λ_{seed}. The microbunched part will emit coherently in the following undulators, called radiator. This radiation mirrors the properties of the seeding radiation with expectation of the wavelength, which can be a harmonic of the seed [27]. However, the quality of the seeded part of the electron bunch suffers from the frequency up-conversion-process.

For the other parts of the bunch the process of density modulation and emission is suppressed, because they are not that strong energy modulated. Nevertheless, these parts are influenced by the emission of synchrotron radiation as well as by the optical features of the lattice.

In the second stage a *new* section of the bunch is used to generate further radiation. The matching of the bunch section and the radiation, which was generated in the first stage, is achieved by a chicane, where the electron bunch is retarded by an loop way through a chicane [29]. In the second stage the FEL process takes place similar to the first stage.

Since the resonance wavelength should be small, high energy electrons are used, e.g. STARS $E = 325\,MeV$ or FLASH II $E = 1.2\,GeV$. Albeit the average particle energy is high in the HGHG-FELs, the length of the magnetic lattice leads a significant impact of space charge force. For example the impact of the longitudinal space charge leads to a reduction of the microbunching. In Genesis1.3 this effect is approached by the model of plasma oscillations.

A criterion of the amplification process in FELs is given by the charge density. In a linear approach space charge effects cause an additional expansion of the bunch, which is escorted by a reduction of the charge density. This leads to a significant impact of the final FEL radiation output power, because the reduction of the radiation output power in the first stage effects also a lower energy modulation in the second stage. In Ref. [28] the dependency of the output radiation power and input radiation power for the simulation of the DUV-FEL is presented. There is a stable region, where small difference in the seed power have almost no effect.

Nevertheless, the impact of space charge of previous sections on the electron bunch are still present in further sections. This is taken into account in the simulations of STARS and FLASH II.

In the following plots the impact of the transverse space charge effects on the properties of the radiation output is presented. For the simulations two different proposed HGHG-FEL-facilities, FLASH II and STARS, are chosen. Parameters of FLASH II are an average particle energy of $1.2\,GeV$ and a maximum peak

current of $1.8\,kA$. In the test facility STARS the average particle energy is about $325\,MeV$, whereby a maximum peak current of more than $0.5\,kA$ is aspired. Note that, in the simulations of FLASH II and STARS longitudinal space charge effects are always taken into account.

5.1 FLASH II

The FLASH II facility is a two-stage HGHG-FEL. The aim resonance wavelength is in the regime of several nanometers, e.g. $4\,nm$. In the following simulations the wavelength of the final radiation output is $8\,nm$. The average particle energy is $1200\,MeV$. In the first stage a planar undulator, characterised by a period length of $80\,mm$ over 20 periods, is used for seeding. The seeding wavelength is $200\,nm$. The radiator of the first stage contains of two undulators. The undulator parameters are: a period length of $62\,mm$, a number of periods of 30 with an undulator parameter of 2.47. Due to the required tunability of the resonance wavelength the fragmentation of the radiator becomes necessary in order to maintain the quality of the radiation output. In the space between the undulators optical elements focus the beam, which leads to a higher output power. Furthermore, the microbunching of the bunch is very important for the radiation process in FELs. The dispersive effects of undulators can be disadvantageous. For longer wavelengths one of the undulators can be turned off, i.e. the gap will be set to the maximum value, whereby the resonance wavelength of the undulator becomes off-resonant to the density modulation of the bunch.

In the following FLASH II simulations both undulators of the first-stage radiator are in use. The resonance wavelength of the first radiator is $40\,nm$. For the seeding process in the second stage the configuration of the modulator is similar to the configuration of the first radiator. The second modulator consists of 25 periods with a period length of $62\,mm$. The second radiator consists of twelve undulators. In the HGHG-mode only some of them are in use. For the following simulation five undulators are in use. The undulator parameters are period length of $29\,mm$, number of periods of 70 and undulator parameter of 1.427. For the simulations the configuration of the radiators corresponds to a planar undulator. Nevertheless, the proposed undulators provide helical configurations as well.

Another mode of FLASH II is SASE. In this mode the gap of all undulators in front of the final radiator are set to the maximum value. Furthermore, all segments of the second radiator are in use, i.e. 12×70 periods. Figure 5.1 shows the schematical layout of FLASH II. The following plots are based on the simulation of FLASH II in the HGHG-FEL mode. In figure 5.2(1) and 5.2(2) the change of the radiation output power of the first stage in dependency of the peak current is illustrated. The absolute power and the relative change produced by space charge are shown. From these plots follows that, even in the high energy regime ($1.2 GeV$) the impact of the transverse space charge can be significant.

Sketch of the cascaded HGHG scheme proposed for FLASH II (the electron beam comes from the right).
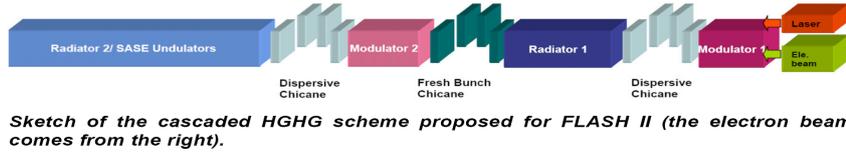
Figure 5.1:   Design FLASH II - HGHG Undulator Section [4]

This figure presents the layout of FLASH II. The electron beam as well as the first-stage seeding-radiation arrive from the right hand side of this scheme.

The transverse space charge effects reduce the final output power. This leads to a lost of radiation power of about 1% at the first stage of FLASH II, simulated with the proposed peak current of $1.8kA$. The development of the radiation power along the radiators of FLASH II are shown in the figure 5.3 and figure 5.4. The relative change of output power is about 1% in the first radiator and about 4.2% in the second radiator.

The difference between the output changes are caused by several facts. The simulation of the second stage radiator bases on the simulation of the first stage, i.e. the relative change of 1% of the radiation output power of the first stage is already included in the seeding progress of the second stage. Furthermore, the space charge induced change of the electron bunch in the first stage is also taken into account. So, the space charge effects cause twice in HGHG-FELs. The impact of space charge on the frequency spectrum is also interesting. In figure 5.5 and 5.6 the frequency spectrums at the end of the first and at the end of the second radiator are presented. From these simulations follow that, the intensity of dominating wavelength seems to be stronger reduced. The differences of the change in the frequency spectrums bases on the accounting of first-stage space-charge effects in the second stage.
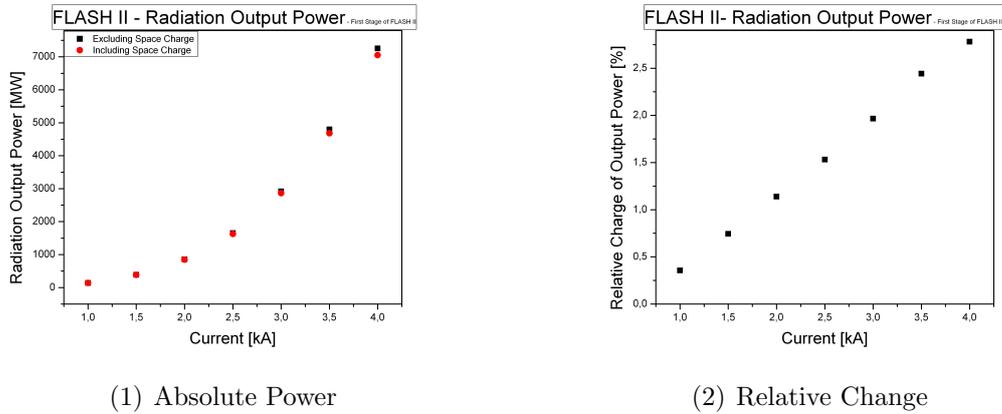
(1) Absolute Power

(2) Relative Change

Figure 5.2:   Radiation Output Power at the First Stage of FLASH II - Absolute
Power(1) and Relative Change(2)
*In the plots the results of the simulation of the first stage of FLASH II including and
excluding space charge effects are shown. The left plot(1) presents the radiation output
power in dependency of the peak current. The relative change produced by space charge
is presented in the right plot(2). It demonstrates, that the impact of space charge is still
significant even at a high energy regime.*
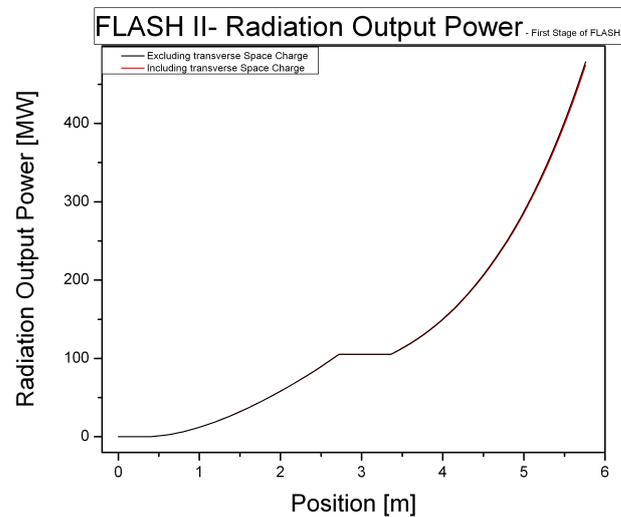
Figure 5.3:   Radiation Output Power at FLASH II - First Stage 1.8 kA Peak Current
*This plot shows the development of the radiation output power along the first radiator.
The change of the final radiation output power is about 1%.*
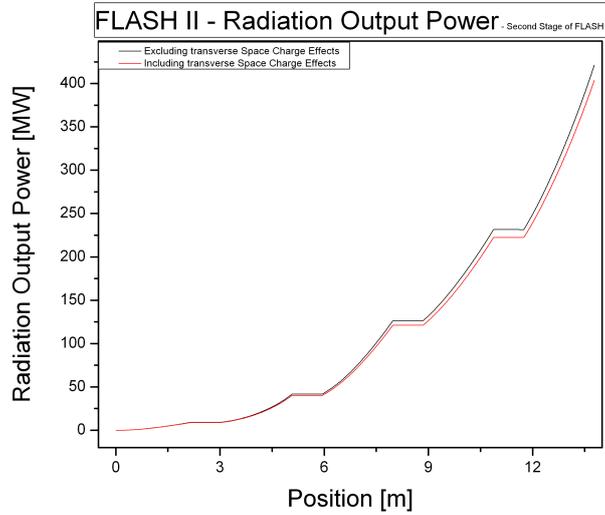
Figure 5.4: Radiation Output Power at FLASHII - Second Stage 1.8 kA Peak Current
*This plot shows the development of the radiation output power along the second radiator.
The impact of space charge from the previous stage is also taken into account. This leads
to a reduction of the final radiation power of about 4.2%.*
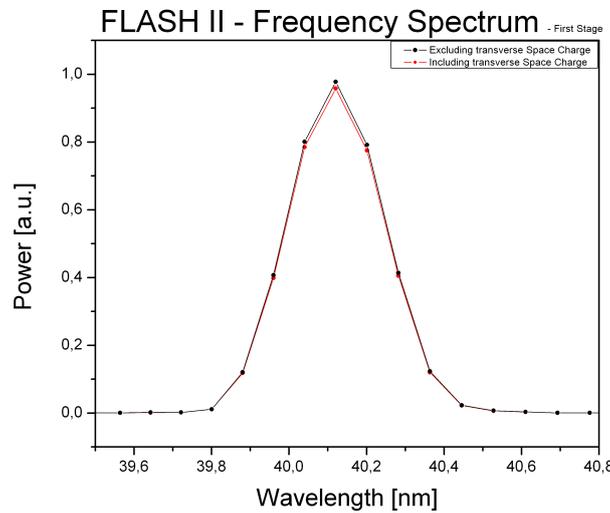
Figure 5.5: Frequency Spectrum at FLASH II - First Stage
*Due to the impact of space charge the radiation output power decreases at all frequencies.
The change is stronger pronounced near the resonance wavelength.*
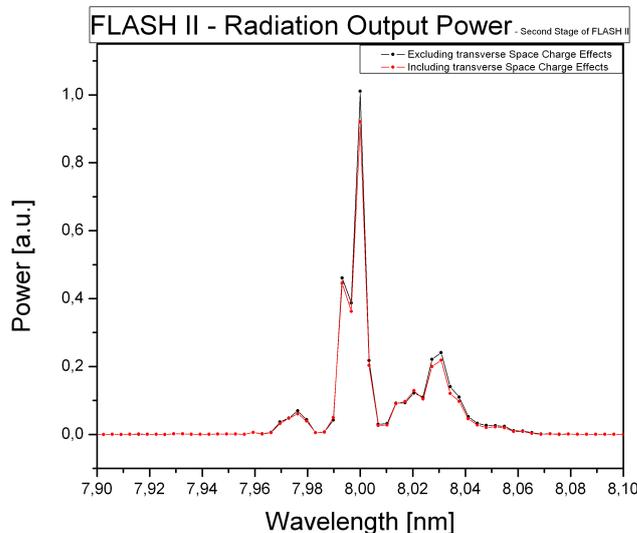
Figure 5.6:   Frequency Spectrum at FLASH II - Second Stage

The impact of space charge reduces the radiation output power at all frequencies. This spectrum contains of two side peaks, where the impact of space charge also cause a reduction.

5.2   STARS

STARS is planned as the test facility for the BESSY-FEL. The average particle energy is $325\,MeV$. A maximum peak current of more than $0.5\,kA$ is expected. For the following simulations the average particle energy is $325\,MeV$ and the peak current is $0.5\,kA$. In the first modulator the electron bunch is seeded with $\lambda_{seed} = 800\,nm$. The undulator parameters are a period length of $50\,mm$, a number of periods of 10 and an undulator parameter of 3.476. In the first stage the radiator consists of two undulators, similar to FLASH II. The undulator parameters are $50\,mm$ period length, 30 periods and 1.27 undulator parameter. This leads to a resonance frequency of $160\,nm$. The radiation output is used to seed the electron bunch in the second stage. The second modulator has a period length of $50\,mm$ over 30 periods with an undulator parameter of 1.27. In the second stage the radiator consists of three undulators. The parameters are a period length of $22\,mm$, a number of periods of 150 and an undulator parameter of 1.26. The resonance frequency of the second radiator is $40\,nm$. Note that, the undulator parameters are tunable and the values above are used for the simulation. The schematical layout of STARS is shown in figure 5.7. In figure 5.8 and 5.9 the development of the radiation output power along the radiators is presented. The change of the first stage radiation output power is about 2.4%, which is higher

than in the case of FLASH II. The peak current in STARS is lower than in FLASH II, but the particle energy is lower as well. In this case the relative change of both parameter is almost the same. This leads to an increased impact of space charge in STARS, because the energy dependency dominates. Figure 5.8 shows the development of the radiation output power along the second radiator. For this simulation the time-independent algorithm of Genesis1.3 is used, where superradiance cannot be calculated.

Since the occurrence of superradiance in the second radiator of STARS is expected, the results of these simulations are only valid outside the superradiance regime. The superradiance regime in figure 5.9 is characterised by the decrease of the radiation output power. A similar development of the radiation output power along the radiator is shown at the time-independent simulation of FLASH II as well. The time-dependent simulation presents a further increase of the radiation output power instead of a decrease, see figure 5.4. Nevertheless, the relative change of the radiation output power at the end of the second radiator accounts already about 13.6 %. A further increase is expected as well. It demonstrates again the significant impact of space charge on the performance of FELs.
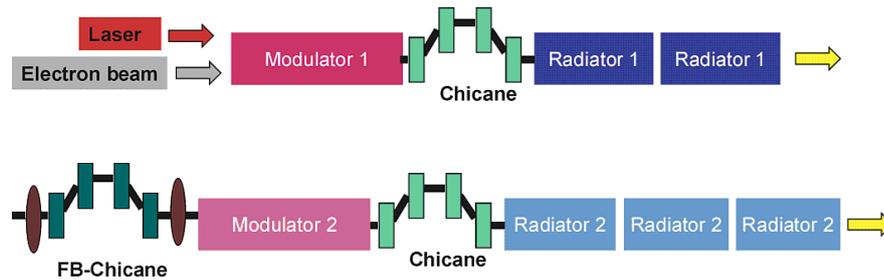
Figure 5.7: Design STARS - HGHG Undulator Section [2]

This figure shows the layout of STARS. The first stage is presented in the upper scheme. The electron beam and the seeding radiation arrive from the left hand side. The lower scheme illustrates the 'fresh bunch' chicane (left chicane) and the second stage.
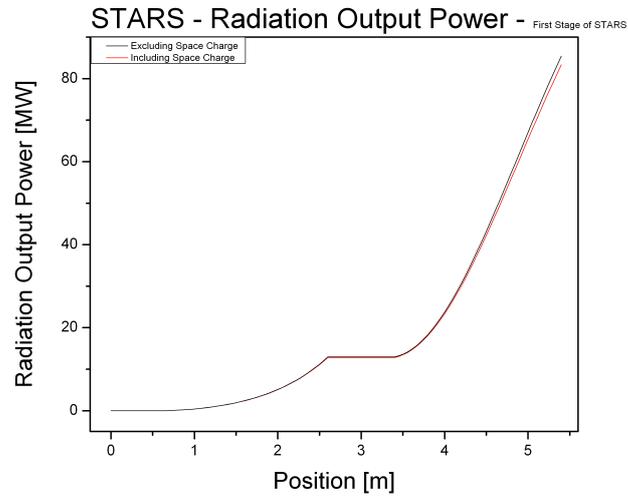
Figure 5.8:   Radiation Output Power at STARS - First Stage 0.5kA Peak Current
This plot shows the development of the radiation output power along the first radiator of STARS. The impact of transverse space charge leads to a reduction of the final radiation output power of 2.4%.
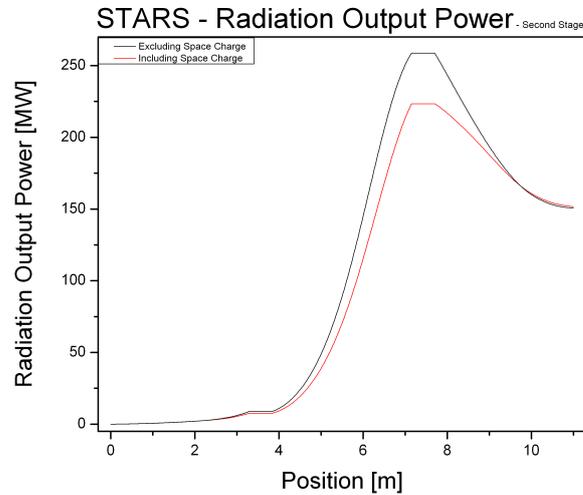
Figure 5.9:   Radiation Output Power at STARS - Second Stage 0.5kA Peak Current
This plot shows the development of the radiation output power along the second radiator of STARS. The occurrence of superradiance is expected at the beginning of the third undulator(7.7m).

5.3   Quadrupole Readjustment

As shown above, the space charge defocusing leads to a reduction of the FEL radiation output. A readjustment of the focusing strength of quadrupoles can be used for the compensation of a dismatch between lattice and beam, which is produced by space charge. For the compensation of the space charge defocusing elements are required, which focus simultaneous in both transversal planes. Therefore, quadrupoles are less suitable for the compensation of the space charge defocusing.

Nevertheless, the readjustment of the focusing strength of quadrupoles can lead to an improvement of the radiation output power. In figure 5.10 the radiation output power at the last part of the first-stage radiator of STARS is presented. In this plot the radiation output power including and excluding space charge along the radiator and the radiation output power including space charge along the radiator with the readjustment are shown. As a result of the readjustment the radiation output power increases. The increase corresponds to 8% of the reduction, which was produced by space charge.
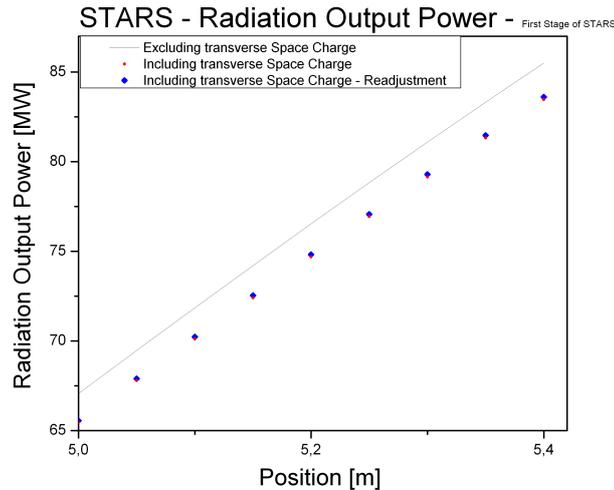
Figure 5.10:   Impact of the Readjustment

In this plot the development of the radiation output power along the last part of the first radiator of STARS is shown. The readjustment of the quadrupole strength leads in an increase of 0.2% of the final radiation output power.

6

Conclusion

FELs offer unique possibilities for many applications in research and development. This is in particular the case for short-wavelength, short-pulse FELs with their high peak-brilliance. The final performance of FELs can suffer from space charge effects. The transverse space charge effects limit the minimum transverse beam size and so the minimum available size of the radiation source. Furthermore, any dismatch between radiation and beam leads to a reduction of the final performance, regardless whether it occurs inside the radiator or inside the modulator.

Simulation programs calculating these effects are essential in order to develop and to investigate the necessary compensation and suppression schemes. Results of such programs are limited by their initial assumptions and approximations, used for computations. The simultaneous employment of different space charge programs, each marked by different assumptions, gives a possibility to investigate the impacts of the space charge effects to different orders. The program P12 is created for fast estimations of the transverse space charge effects in multi-cascade FELs, like STARS and FLASH II.

In the present work, the theoretical background underlying the code P12 is discussed. In this connection the model of the 'equivalent uniform beam' is introduced. This model is available, because the development of the second moment of different charge distributions demonstrate similar behaviour. Real charge distributions are approached by an uniform charge model. Thus, the space charge effects can be estimated without the use of particle tracking. The implementation of the space charge effects in programs including special features of coupling elements is also discussed.

In the fourth chapter the results of the program P12 are benchmarked with those of established programs. The results including and excluding space charge effects fits to the results of the other programs. Furthermore, the expected small differences, which are based on the different initial assumptions and approximations, have occurred as well. The results presented in this chapter demonstrates not only the reliability of the program P12, but it also presents the need of accounting space charge in the simulation of FEL performances.

In context of this work, the transversal space charge defocusing was implemented in the code Genesis1.3 to provide the chance to estimate the impact of the transversal space charge effects on the final FEL radiation output. The space charge effects causes an additional defocusing of the electron bunch, which leads to a reduction of the charge density and so to a reduction of the final radiation

output power of FELs. In the case of HGHG-FELs the space charge effects are particular important, because the performance of further stages depends on the quality of the radiation output of previous stages. So, space charge effects escalate in HGHG-FELs.

In the fifth chapter the results of the FEL-simulations of two proposed FEL-facilities, STARS and FLASH II, are shown. The results of these simulations demonstrate, that even in a high energy regime space charge effects can cause a significant change in the performance of FELs. Thus, space charge effects have to be taken into account for the valid estimation of the performances of FELs. Nevertheless, compensation schemes will reduce the loss of performance.

Some elements tend to couple different space charge effects, e.g. coupling of transverse and longitudinal space charge force in bends, it is necessary to consider this coupling. Therefore, it could be positive to update the program P12 with subroutines for the calculation of longitudinal space charge effects. This will provide the possibility to use P12 during the design phase of the future project BESSY-ERL.

Appendix A
Particle Optics

Introduction

The effect of electro-magnetic fields on charged particles, like electrons, is described by the Lorentz equation. Due to these fields, particles can be forced on designed trajectories in accelerators. In high energy accelerators, like BESSYII, PETRA III, MLS, FLASH, where the particles become relativistic, the Lorentz equation reads as :

$$\vec{F}_L = q \cdot (\vec{E} + c \cdot \vec{\beta} \times \vec{B}) \text{ with } \vec{\beta} = \frac{\vec{v}}{c} \tag{A.1}$$

Due to the generation process and collective effects inside the beam, the particle beam has a divergence. Hence, the beam has to be focused. A development of beam optics with focusing elements is described in [9].

Elements of Linear Beam Optics

This subsection presents elements involved in the code P12. Results will be shown and discussed in the reference coordinate system [9]. The particles are assumed to be relativistic.

Drifts

According to Newton's laws, if the sum of all force influencing a particle yields zero then the particle will rest or move with a constant velocity vector. The drift is the simplest element in accelerator physics. A drift describes a space without any external fields. Thus, a particle moves without external influences and its individual velocity and its propagation vector remains constant. There is no coupling between the different planes and the planes can be treated in a separated manner.

If the momentum of the particle differ from the momentum of the reference particle, the drift will have an effect on the particle displacement. The special coordinate system used in accelerator physics simplifies the problem. Assuming, the initial particle coordinates in phase space are (a_1, a_1'), the final displacement after a drift length L becomes :

$$a_1(L) \quad = \quad a_1(0) + L \cdot a_1'(0). \tag{A.2}$$

Since the propagation vector is constant, a'_1 remains constant.

$$a'_1(L) \;=\; 0 + a'_1(0). \tag{A.3}$$

The effect of drifting can be expressed by a matrix formula

$$\begin{pmatrix} a_1(L) \\ a'_1(L) \end{pmatrix} \;=\; M \cdot \begin{pmatrix} a_1(0) \\ a'_1(0) \end{pmatrix} \tag{A.4}$$

$$\text{with } M \;=\; \begin{pmatrix} 1 & L \\ 0 & 1 \end{pmatrix} \tag{A.5}$$

For a relativistic particle the longitudinal plane has to be modified by the Lorentz-transformation. The full 6×6 -matrix is:

$$M = \begin{pmatrix} 1 & L & 0 & 0 & 0 & 0 \\ 0 & 1 & 0 & 0 & 0 & 0 \\ 0 & 0 & 1 & L & 0 & 0 \\ 0 & 0 & 0 & 1 & 0 & 0 \\ 0 & 0 & 0 & 0 & 1 & \frac{L}{\gamma^2} \\ 0 & 0 & 0 & 0 & 0 & 1 \end{pmatrix} \tag{A.6}$$

The following representation illustrates the effect of drifts.
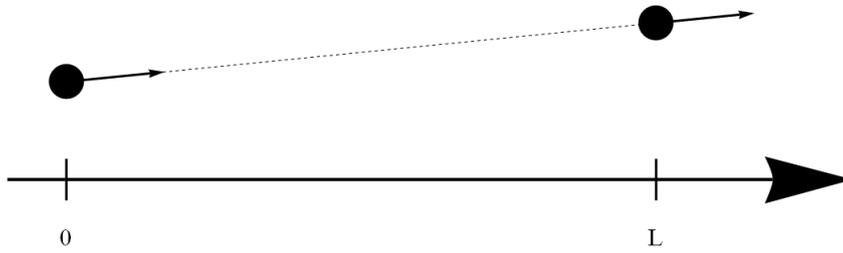
Figure A.1:   Impact of a Drift

The impact of a drift is a displacement, where the propagation vector remains constant.

Bending Magnets

Bending Magnet - Sbend

The Sbend is a special kind of bending magnet. Due to its special design the beam perpendicularly enters the element. The impact of the bending field starts simultaneous along the hole bunch cross section.
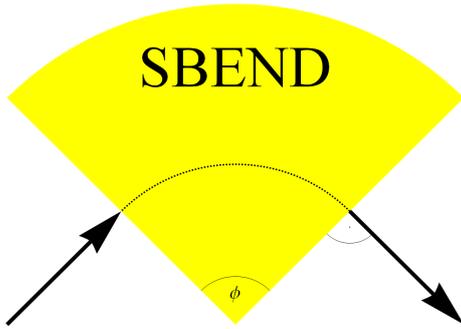
Figure A.2:   Sbend

This figure shows the diagram of a Sbend. The particle beam enters and leaves the magnetic field perpendicular.

The equations of motion (eq.2.1, eq.2.2) for a pure Sbend, bending in xz-plane, simplify to:

$$x''(s) + \frac{1}{R^2(s)}x(s) = \frac{1}{R(s)}\frac{\Delta p}{p},$$
$$y''(s) = 0.$$

In the non-bending plane the development of the particle beam is similar to the development in a drift section. In the bending plane a focusing effect occurs, so-called 'weak' focusing.

This focusing effect is based on the approach of particle paths inside a bending magnet. It is illustrated below. Two identical, charged particles pass the bending magnet. The paths are marked by their colours, blue and black. In the figure A.3 the two paths approach each other and cut.
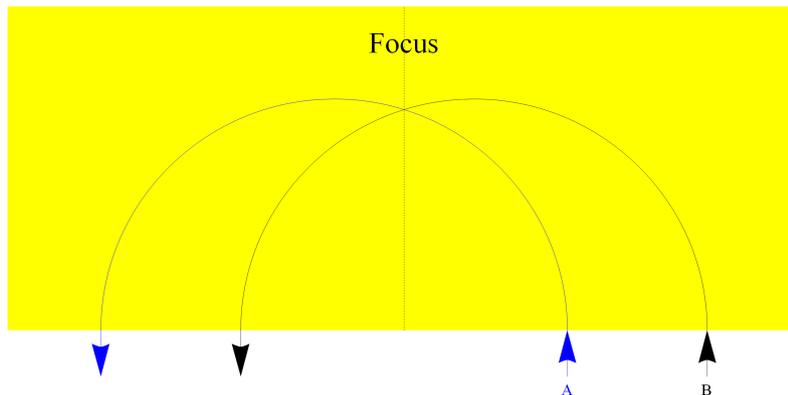
Figure A.3:   Weak Focusing

The weak focusing is an effect, which is based on the rotation of the bunch inside a bend.

An approach for the solution of the homogeneous differential equation is:

$$x = A\cos(\frac{s}{R}) + B\sin(\frac{s}{R}),$$
$$x' = -\frac{A}{R}\sin(\frac{s}{R}) + \frac{B}{R}\cos(\frac{s}{R}).$$

The boundary conditions are set to $x(0) = x_0$ and $x'(0) = x_0'$. This leads to:

$$\left(\begin{array}{c} x(s) \\ x'(s) \end{array} \right) = \left(\begin{array}{cc} \cos(\frac{s}{R}) & R \cdot \sin(\frac{s}{R}) \\ \frac{1}{R} \cdot \sin(\frac{s}{R}) & \cos(\frac{s}{R}) \end{array} \right) \cdot \left(\begin{array}{c} x(0) \\ x'(0) \end{array} \right).$$

In the case of $\frac{\Delta p}{p} \neq 0$, i.e. the particle is characterised by a momentum deviation, the particle moves on a dispersion path $(D(s))$. In linear optics dispersion takes place , if $\frac{1}{R} \neq 0$ (eq.s 2.1 and eq. 2.2). The differential equation of the dispersive path is:

$$D''(s) + \frac{1}{R^2}D(s) = \frac{1}{R}, \tag{A.7}$$

solves to give:

$$D(s) = A\cos(\frac{s}{R}) + B\sin(\frac{s}{R}) + R,$$
$$D'(s) = -\frac{A}{R}\sin(\frac{s}{R}) + \frac{B}{R}\cos(\frac{s}{R}),$$
$$D''(s) = -\frac{1}{R^2}(A\cos(\frac{s}{R}) + B\sin(\frac{s}{R})).$$

For initial conditions: $D(0) = D_0$ and $D'(0) = D_0'$, it results in :

$$A = D_0 - R,$$
$$B = D_0' \cdot R.$$

The equation of dispersion leads to:

$$D(s) = (D_0 - R)\cos(\frac{s}{R}) + D_0'R\sin(\frac{s}{R}) + R,$$
$$= D_0\cos(\frac{s}{R}) + D_0'\sin(\frac{s}{R}) + R(1 - \cos(\frac{s}{R})), \tag{A.8}$$
$$D'(s) = -\frac{D_0}{R}\sin(\frac{s}{R}) + D_0'\cos(\frac{s}{R}) + \sin(\frac{s}{R}). \tag{A.9}$$

In the longitudinal plane, a effect similar to dispersive effects occurs, which leads to a change of the position along the bunch in dependency of the momentum deviation. This is discussed in more detail in [9].
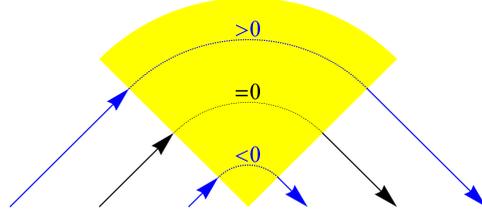
Figure A.4: Dispersive Effect

Particles with different momentums move on different paths, whereby a higher momentum is related to a larger radius.

In summary the effect of Sbends is expressed by the following matrix:

$$(A.10)$$

$$
R_{Sbend} = \begin{pmatrix}
cos(\frac{s}{R}) & Rsin(\frac{s}{R}) & 0 & 0 & 0 & R(1 - cos(\frac{s}{R})) \\
\frac{-1}{R}sin(\frac{s}{R}) & cos(\frac{s}{R}) & 0 & 0 & 0 & sin(\frac{s}{R}) \\
0 & 0 & 1 & s & 0 & 0 \\
0 & 0 & 0 & 1 & 0 & 0 \\
-sin(\frac{s}{R}) & -R(1 - cos(\frac{s}{R})) & 0 & 0 & 1 & -\frac{s}{\gamma^2} + (Rsin(\frac{s}{R}) - s) \\
0 & 0 & 0 & 0 & 0 & 1
\end{pmatrix}.
$$

Edge Focusing - Thin Lens Approximation

If the beam did not enter perpendicular the field of a bending magnet, an additional effect occurs, which influences the beam divergence. This effect can be simulated by introducing an additional 'magnetic wedge' [23].
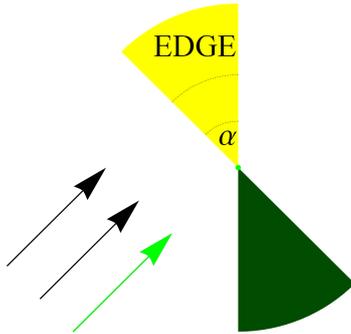
Figure A.5: Edge Focusing

Particle with transverse displacement take a different path through the magnetic field. This path length difference causes the focusing effect.

The path length deviation in a bending magnet for a particle with the displacement $x = x_0$ amounts to:

$$\Delta l = x_0 tan(\alpha). \qquad (A.11)$$

A different path length inside a bending magnet causes a different change of the propagation vector. Any difference in the length of paths can be transformed into an angle(Δ):

$$\Delta = \frac{\Delta l}{R} = x_0 \frac{tan(\alpha)}{R}. \qquad (A.12)$$

Particles, which enter the yellow part of the edge, experience an additional bending. Particles in the green part experience the inverse effect of bending. Edges

are used to be combined with bends. The transfermatrix of an edge is:

$$M_{edge} = \begin{pmatrix} 1 & 0 & 0 & 0 & 0 & 0 \\ \frac{tan(\alpha)}{R} & 1 & 0 & 0 & 0 & 0 \\ 0 & 0 & 1 & 0 & 0 & 0 \\ 0 & 0 & -\frac{tan(\alpha)}{R} & 1 & 0 & 0 \\ 0 & 0 & 0 & 0 & 1 & 0 \\ 0 & 0 & 0 & 0 & 0 & 1 \end{pmatrix} \tag{A.13}$$

Bending Magnet - Rbend

In contrast to the Sbends, particles do not enter and leave perpendicular the magnet field of a Rbend. Rbends can be modelled by a combination of two edges and one Sbend.
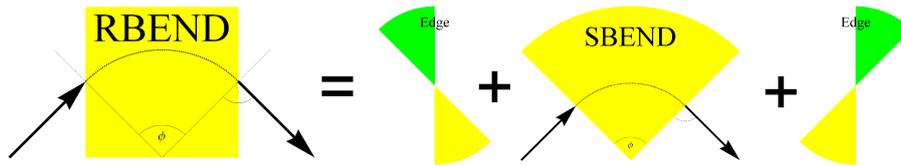
Figure A.6:   Rbend - Calculation Scheme

This scheme shows the calculation algorithm of Rbends. A Rbend consists of a Sbend part and two Edges, whereby angles of the two edges can differ from each other.

As a result of the edges, the particles change their propagation vectors before entering and after leaving the Sbend part. In Rbends the 'weak-focusing' of the Sbend is totally compensated by the 'edge-focusing', if the sum of the two angles of the edges corresponds to the bending angle of the Sbend part. In summary, a Rbend can focus in the opposite plane of bending, but the dispersion remains identical to the dispersion of the Sbend.

Quadrupole Magnets

The focusing of radiation can be realised by lenses. Inside the lens the propagation velocity of light decreases. Thus, the surface of constant phase can be changed and the beam becomes focused or defocused.

The focusing of charged particles differs. Charged particles become focused by special field configurations. The Quadrupole is one of these configurations. The quadrupole field is marked by a constant field gradient:

$$\frac{dB_y}{dx} = \frac{p}{q} \cdot k = \text{constant}. \tag{A.14}$$
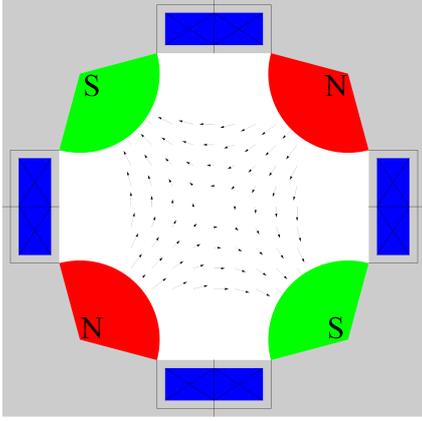
Figure A.7: Quadrupole Design

p is momentum of particle, *q* is charge of particle and *k* is focusing strength of the quadrupole. This is a schematic plot of a quadrupole cross section. Four coils (blue caskets) generate four magnetic poles (marked by red and green). The arrows symbolise the magnetic field direction. E.g. if electrons move out from the picture plane, they become focused in the vertical plane and defocused in the horizontal plane. For particles with the opposite propagation direction, the focusing and the defocusing plane have changed.

Two magnetic pole pairs generate the field configuration of a quadrupole. Quadrupoles are used to focus particle beams, to pin single atoms, etc. .

The equation of motion for particles in quadrupoles is given by eq.2.1 and eq.2.2. In the following example the quadrupole focuses in the yz-plane. The equations of motion are:

I $x'' - k_x \cdot x = 0,$

solves to give:

$$x(s) = A \cdot sinh(\sqrt{k_x}x) + B \cdot cosh(\sqrt{k_x}x),$$
$$x'(s) = \sqrt{k_x}(A \cdot cosh(\sqrt{k_x}x) + B \cdot sinh(\sqrt{k_x}x)),$$
$$x''(s) = k_x(A \cdot sinh(\sqrt{k_x}x) + B \cdot cosh(\sqrt{k_x}x)),$$

with boundary conditions: $x(0) = x_0$ and $x'(0) = x'_0$

$$\Rightarrow x(s) = x_0 \cdot cosh(\sqrt{k_x}s) + \frac{x'_0}{\sqrt{k_x}} \cdot sinh(\sqrt{k_x}s)$$

II $y'' + k_y \cdot y = 0$

solves to give:

$$y(s) = A \cdot sin(\sqrt{k_y}y) + B \cdot cos(\sqrt{k_y}y)$$
$$y'(s) = \sqrt{k_y}(A \cdot cos(\sqrt{k_y}y) - B \cdot sin(\sqrt{k_y}y))$$
$$y''(s) = -k_y(A \cdot sin(\sqrt{k_y}y) + B \cdot cos(\sqrt{k_y}y))$$

boundary conditions: $y(0) = y_0$ and $y'(0) = y'_0$

$$\Rightarrow y(s) = y_0 \cdot cos(\sqrt{k_y}s) + \frac{y'_0}{\sqrt{k_y}} \cdot sin(\sqrt{k_y}s)$$

The element R_{56} is defined by $\frac{lqF}{\gamma^2}$, where lqF corresponds to the longitudinal dimensions of the quadrupole. So, the transfermatrix results in:

$$(A.15)$$

$$
\begin{pmatrix}
cosh(\varphi_x) & \frac{1}{\sqrt{|k_x|}}sinh(\varphi_x) & 0 & 0 & 0 & 0 \\
\sqrt{|k_x|}sinh(\varphi_x) & cosh(\varphi_x) & 0 & 0 & 0 & 0 \\
0 & 0 & cos(\varphi_y) & \frac{1}{\sqrt{|k_y|}}sin(\varphi_y) & 0 & 0 \\
0 & 0 & -\sqrt{|k_y|}sin(\varphi_y) & cos(\varphi_y) & 0 & 0 \\
0 & 0 & 0 & 0 & 1 & \frac{lqF}{\gamma^2} \\
0 & 0 & 0 & 0 & 0 & 1
\end{pmatrix}
$$

with $\varphi_i = \sqrt{|k_i|}lqF$, which corresponds to the phase.

Appendix B

RMS Value

Different distributions $f(x)$ are characterises by their moments. The first moment of a distribution is the expectation value $E(f)$. It is:

$$< x > = E(f) \quad = \quad \int\limits_{-\infty}^{\infty} x f(x) \mathrm{d}x. \tag{B.1}$$

The second moment of a distribution is also known as the variance $V(f)$. It describes the statistical scattering or the root mean square (RMS) value. It is defined by the expectation value:

$$V(f) \quad = \quad \int\limits_{-\infty}^{\infty} (E(x) - x)^2 f(x) \mathrm{d}x. \tag{B.2}$$

If the expectation values of a distribution vanishes, then eq.B.2 becomes:

$$V(f) \quad = \quad \int\limits_{-\infty}^{\infty} x^2 f(x) \mathrm{d}x. \tag{B.3}$$

Note, that the distributions f is normalised.

charge distribution

The equivalent beam model bases on the following charge distribution, which was introduced for the space charge calculations. In this model a homogeneous distribution is assumed. The profile function, $A(x)$ implies the boundary conditions of the distribution:

$$A(x) \quad = \quad A_0(1 - \frac{x^2}{a^2}), \tag{B.4}$$

where a is the maximum extension of the distribution and A_0 is the normalisation factor, which is determined by:

$$1 \quad = \quad \int\limits_{-a}^{a} A_0(1 - \frac{x^2}{a^2}) \mathrm{d}x = A_0 \frac{4a}{3}.$$

The second moment becomes:

$$\sigma_x^2 \;=\; \int\limits_{-\infty}^{\infty} A_0 x^2 (1 - \frac{x^2}{a^2})\mathrm{d}x = \frac{a^2}{5},$$

$$\Rightarrow \; a \;=\; \sqrt{5}\sigma_x. \qquad\qquad (\mathrm{B.5})$$

Hence it follows, that the borders of the equivalent beam corresponds to $\sqrt{5}$ the second moment of the exact distribution. Two further distributions are of interest, because they are often used in approaches in accelerator physics. The first one is a double Θ-function. E.g. in photo-rf-guns the profile of an electron bunch a modelled by a flat top model, which corresponds to a double Θ-function. This profile is generated by the radiation, which is used to generate the bunch.

Double-Θ-function
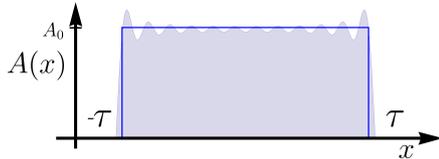
Figure B.1: Double-Θ-function

In Photo-rf-guns short radiation pulses are used to generate electron bunches. A model of the profile of such pulses is shown in this figure.

The profile function is defined by:

$$A(x) \;=\; A_0(\Theta(x + \tau) - \Theta(x - \tau)),$$

$$\Rightarrow \; A_0 \;=\; \frac{1}{2\tau}.$$

The second moment of the double-Θ-function is:

$$\sigma_x = \frac{\tau}{\sqrt{3}}.$$

Gauss-function
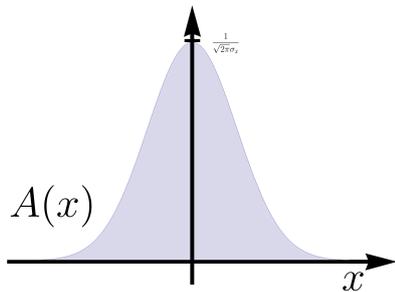
Figure B.2: Gaussian Function

The profile of electron bunches in storage rings can be approached by a gaussian function.

The Gauss-function is defined by its RMS-value:

$$A(x) \;=\; A_0 e^{-\frac{x^2}{2\sigma_x^2}},$$

$$\Rightarrow \; A_0 \;=\; \frac{1}{\sqrt{2\pi}\sigma_x}.$$

The second moment is already known directly from the distribution.

Appendix C
The Triaxial Ellipsoid

This appendix is a summary of the calculation of field distributions of an uniform charged triaxial ellipsoid. In the first part the special coordinate system is presented. In the second part a short summary of the calculation of the field distributions [18] follows.

Coordinate System

It is convenient to choose a coordinate system suitable to the task. Due to the symmetry of the triaxial Ellipsoid the elliptical coordinates seem to be suitable:

$$
\begin{aligned}
x &= a \cdot r \cdot sin(\theta)cos(\varphi), \\
y &= b \cdot r \cdot sin(\theta)sin(\varphi), \\
z &= c \cdot r \cdot cos(\theta).
\end{aligned}
$$

This approach yields to very complex elliptical integrals. Another more handy approach presented below uses specific coordinates, which are determined by the boundary of the ellipsoid:

$$
\frac{x^2}{a^2} + \frac{y^2}{b^2} + \frac{z^2}{c^2} = 1. \tag{C.1}
$$

For the determination of the new coordinates the following two functions are required:

$$
\begin{aligned}
f(s) &= \frac{x^2}{a^2 + s} + \frac{y^2}{b^2 + s} + \frac{z^2}{c^2 + s} - 1 \tag{C.2} \\
\varphi(s) &= (a^2 + s)(b^2 + s)(c^2 + s) \tag{C.3}
\end{aligned}
$$

The zeros of the second equation (C.3) present poles of the first eq. (C.2). $f(s)$ characterises the profile function of ellipsoids in dependency of s. If s is larger than a, b and c it describes the profile of an ellipsoid. If s is smaller than a or b or c it describes the profile of a hyperboloid and else the hyperboloid splits up into two parts. In the case of $s = 0$ $f(s)$ becomes the profile function of the original ellipsoid.

The new coordinates are functions of the zeros(ν, μ, λ) of:

$$f(s) \cdot \varphi(s) = 0 \tag{C.4}$$
$$-(s - \lambda)(s - \mu)(s - \nu) = x^2(b^2 + s)(c^2 + s) + y^2(a^2 + s)(c^2 + s)$$
$$+z^2(a^2 + s)(b^2 + s) - \Phi(s)$$

The left hand side of eq.C.4 results from the mathematical boundary conditions, which requires three real roots. For the determination of the coordinates depending on the properties of the ellipsoid the variable 's' has to be eliminated. While plugging in $-a^2, -b^2$ and $-c^2$ for 's' in eq. C.4, $\Phi(s)$ and two of the three 'old' coordinates (x, y, z) always vanish. Thus the 'old' coordinates are replaced by functions of ν, μ and λ as well as a, b and c:

$$x = \frac{(a^2 + \lambda)(a^2 + \mu)(a^2 + \nu)}{(a^2 - b^2)(a^2 - c^2)}, \tag{C.5}$$

$$y = \frac{(b^2 + \lambda)(b^2 + \mu)(b^2 + \nu)}{(b^2 - a^2)(b^2 - c^2)}, \tag{C.6}$$

$$z = \frac{(c^2 + \lambda)(c^2 + \mu)(c^2 + \nu)}{(c^2 - a^2)(c^2 - b^2)}. \tag{C.7}$$

Field Distribution of an Uniform Charged Ellipsoid

In the case of an electrostatic problem the electric field can be expressed as the gradient of the electrostatic potential $\Phi(\vec{r})$:

$$\vec{E} = -\nabla\Phi. \tag{C.8}$$

In general this potential is given by:

$$\Phi(\vec{r}) = \frac{1}{4\pi\epsilon_0} \int \frac{\varrho(\vec{r'})}{|\vec{r} - \vec{r'}|} \mathrm{d}^3 r'. \tag{C.9}$$

For a uniform charge distribution the charge density can be extracted form inside the integral. Due to the special coordinates eq. C.9 becomes:

$$\Phi_u = 2\pi abc\varrho_0 u^3 \int_{\lambda(u)}^{\infty} \frac{\mathrm{d}s}{\sqrt{\varphi(u, s)}}. \tag{C.10}$$

Note, that in the following the cgs-unit-system is used, i.e. $4\pi\epsilon_0$ is set to 1. In the eq. C.10 'u' presents a kind of radius. The length of the semi-axis of the ellipsoid scales with u to $a \cdot u, b \cdot u$ and $c \cdot u$. $\lambda(u)$ stands for the greatest root of eq. C.2 with scaled semi axis $(a \cdot u, \ldots)$. Due to the special choice of variables two different potential regimes have to be distinguished. Each set of a, b and c presents

a family of similar ellipsoids. The eq. C.10 describes the potential at a special orbital depending on u. The potential in the point $\vec{r}$ is connected with the *radius* u_0. For the determination of the potential in the point $\vec{r}$ the hole volume has to be taken into account, which results a singularity at $u = u_0$ (eq. C.9). So inside the ellipsoid the integration over 'u' has to split into two parts. To cover the hole volume the integration reaches from 0 to u_0 and from u_0 to 1. Due to a change of the integration variable the function φ becomes independent of u, which allows the separated integrations.

$$s = u^2 t \quad \Rightarrow \quad \mathrm{d}s = u^2 \mathrm{d}t \quad \text{and} \quad \lambda = u^2 \nu \tag{C.11}$$

$$\Rightarrow \quad \varphi(u, s) = \varphi(t) \cdot (u^2)^3 \tag{C.12}$$

As reminder, the coordinate u determines the size of the ellipsoid, thus its meaning in these coordinate system is similar to the meaning of the radius in the spherical coordinate system.

$$u^2 = \frac{x^2}{a^2 + s} + \frac{y^2}{b^2 + s} + \frac{z^2}{c^2 + s}$$

The potential becomes:

$$\Phi_i = 2\pi abc\varrho_0 \int_0^1 u^2 \int_{\lambda(u)}^{\infty} \frac{\mathrm{d}s}{\sqrt{\varphi(u, s)}} \mathrm{d}u$$

$$= 2\pi abc\varrho_0 \left(\int_0^{u_0} u \int_{\nu}^{\infty} \frac{\mathrm{d}l}{\sqrt{\varphi(l)}} \mathrm{d}u + \int_{u_0}^1 u \int_0^{\infty} \frac{\mathrm{d}l}{\sqrt{\varphi(l)}} \mathrm{d}u \right)$$

$$\vdots$$

$$= \pi abc\varrho_0 \int_0^{\infty} \left(1 - \frac{x^2}{a^2 + s} - \frac{y^2}{b^2 + s} - \frac{z^2}{c^2 + s} \right) \frac{\mathrm{d}s}{\sqrt{\varphi(s)}}. \tag{C.13}$$

A separation of the different parts within the brackets leads to separated expressions for each direction. The potential simplifies to:

$$\Phi_i = -Ax^2 - By^2 - Cz^2 + D. \tag{C.14}$$

Hence it follows, the electric field inside the ellipsoid depends linear on position:

$$\vec{E}_i = 2A\vec{x} + 2B\vec{y} + 2C\vec{z}. \tag{C.15}$$

A, B, C and D are constant and depend on the parameters of the ellipsoid:

$$A = \pi abc\varrho_0 \int_0^{\infty} \frac{\mathrm{d}s}{(a^2 + s)\sqrt{\varphi(s)}},$$

$$B = \pi abc\varrho_0 \int_0^\infty \frac{\mathrm{d}s}{(b^2 + s)\sqrt{\varphi(s)}},$$

$$C = \pi abc\varrho_0 \int_0^\infty \frac{\mathrm{d}s}{(c^2 + s)\sqrt{\varphi(s)}},$$

$$D = \pi abc\varrho_0 \int_0^\infty \frac{\mathrm{d}s}{\sqrt{\varphi(s)}}.$$

Bibliography

[1] D.Krämer, E.Jeaschke and W.Eberhardt (editors). The bessy soft x-ray free electron laser, 2004. ISBN 3-9809534-0-8.

[2] J.Knobloch, E.Jeaschke and W.Eberhardt (editors). STARS, proposal for the construction of a cascaded hghg fel. *BESSY report, Berlin, Germany*, 2006.

[3] Proposal for FLASH II. http://flash.desy.de/flashii, 2009.

[4] Atoosa Meseck. Private Communication, 2008/2009.

[5] Introduction to FELIX. FOM-Institute for Plasma Physics Rijnhuizen. http://www.rijnh.nl/research/guthz/felix_felice, 2009.

[6] G.Grübel et al. XPCS at the european x-ray free electron laser facility. *Nucl. Instrum. Meth.*, B262:357-367, 2007

[7] S.Eisebitt. X-ray holography: the hole story. *Nature Photonics*, 2:529-530, 2008

[8] S.Reiche. Numerical studies for a single pass high gain free-electron-laser. DESY-Thesis-2000-012.

[9] K.Wille. Physik der Teilchenbeschleuniger und Synchrotronstrahlungs- quellen. *Teubner Studienbücher Stuttgart*, 1992 .

[10] A.Septier (editor). Focusing of charged particles, volume II. *Academic Press New York, San Francisco, London*, 1967.

[11] S.Sasaki, K.Miyata, T.Takada. A new undulator for generating variably po- larized radiation. *Japanese Journal of Applied Physics, Part 2, Volume 31, no12B:L1794-L1796*, 1992.

[12] J.Bahrdt, M.Scheer, G.Wüstefeld. Tracking simulations and dynamic multi- pole shimming for helical undulators. *Proc. of the EPAC*, 2006.

[13] G.Wüstefeld, M.Scheer. Canonical particle tracking and end pole matching of helical insterion devices. *Proc. of the PAC* , 1997.

[14] J.D.Jackson. Klassische Elektrodynamik. *Walter de Gruyter Berlin New York (2. Auflage)*, 1983.

[15] K.Schindl. Space charge. *CAS, Cern, p.305-320*, 2003.

[16] M.Reiser. Theory and design of charged particle beams. *Wiley Series in Beam Physics and Accelerator Technology*, 1994.

[17] P.M.Lapostolle. Effets de la charge d'expace dans un accelerateur a protons. *Cern Libraries, Geneva, Sg/65-15*, 1965.

[18] O.D.Kellogg. Foundations of potential theory. *Springer Verlag, Berlin*, 1976.

[19] Bronstein, Semendjajew, Musiol, Mühlig. Taschenbuch der Mathematik. *Verlag Harri Deutsch, Thun und Frankfurt/Main (5.Auflage)*, 2001.

[20] M.R.Shubaly. Space charge fields of elliptical symmetrical beams. *Nucl. Instrum. Meth., 130:19-21*, 1975.

[21] C.K.Allen and N.D.Pattengale. Theory and techique of beam envelope simulation. *Los Alamos National Laboratory (LA-UR-02-4979)*, 2002.

[22] K.R.Crandall and D.P.Rushoi. Trace 3-D Documentation (Third Edition). *Los Alamos National Laboratory*, 1997.

[23] J.Rossbach and P.Schmüser. Basic Course on Accelerator Optics. *CAS, Cern*, 1993.

[24] F.Hinterberger. Physik der Teilchenbeschleuniger und Ionenoptik. *Springer Verlag Berlin u.a.*, 1997.

[25] Michael Scheer. Private Communication, 2009.

[26] E.L.Saldin, E.A.Schneidmiller, M.V.Yurkov.The Physics of Free Electron Lasers. *Springer Verlag Berlin u.a.*, 2000.

[27] Li-Hua Yu et al. First ultraviolet high-gain harmonic-generation free-electron laser. *Physical Review Letters 91, 074801*, 2003.

[28] Li-Hua Yu and J.Wu. Theory of high gain harmonic generation: an analytical estimate. *Nucl. Instrum. Meth., A483:493-498*, 2002.

[29] Li-Hua Yu and I. Ben-Zvi. High-gain harmonic generation of soft x-rays with the fresh bunch technique. *Nucl. Instrum. Meth. A393: 96-99*, 1997.

Acknowledgment

First of all, I would like to thank Prof. Eberhard Jaeschke, my thesis advisor, for his support, for providing me the opportunity to write this thesis at BESSY/HZB and for examining it.

Furthermore, I would like to thank Prof. Shaukat Khan for serving as the second consultant.

I am indebted to Atoosa Meseck. She encouraged my interest in accelerator physics and FEL physics. Beyond that, I would like to thank her for supervising the progress of this thesis, for the close cooperation and for the response of all questions I had.

I thank Alexander N. Matveenko for the many fruitful discussions and for the assistance in handling Trace3D.

I also would like to thank the other members of the BESSY community for their cooperation and for the pleasant working atmosphere, especially, Rolf Mitzner, Michael Scheer, Johannes Bahrdt, Godehard Wüstefeld, Jörg Feikes, Bettina Kuske, Nikoline Hansen, Thorsten Kamps, Torsten Quast and Wolfhart Woywode.

I also give props to Torsten Leitner, Sandra Fischer, Terry Atkinson and Heike Christopher for reading this thesis. A special thanks goes to Torsten Leitner, who assists with good LaTeX tips.

Finally, I thank my family and my friends for their encouragement and their support.

Erklärung

Hiermit erkläre ich, dass ich die Diplomarbeit selbständig verfasst und keine anderen als die angegebenen Quellen und Hilfsmittel verwendet habe.
Ich bin mit der Auslage meiner Diplomarbeit in den Bibliotheken der Humboldt-Universität zu Berlin einverstanden.

Berlin, den 20. April 2009

Lutz Hein